Journal of CO2 Utilization 70 (2023) 102428

Contents lists available at ScienceDirect

Journal of CO2 Utilization

journal homepage: www.elsevier.com/locate/jcou

Investigation of Cu/TiO_2 synthesis methods and conditions for CO_2 photocatalytic reduction via conversion of bicarbonate/carbonate to formate

Abdullahi Adamu [a], Mark Isaacs [b,c], Kamelia Boodhoo [a], Fernando Russo Abegão [a,*]

[a] School of Engineering, Faculty of Science, Agriculture and Engineering, Newcastle University, Newcastle upon Tyne NE1 7RU, UK
[b] Harwell XPS, Research Complex at Harwell, RAL, Oxfordshire OX11 0FA, UK
[c] Department of Chemistry, University College London, London WC1H 0AJ, UK

ARTICLE INFO

Keywords:
Titania
Band offset
CO_2 reduction
Photocatalysis
Copper-doping

ABSTRACT

This work is aimed at improving the photocatalytic activity of TiO_2 in the reduction of CO_2. TiO_2 and Cu/TiO_2 at 5 wt% copper bulk loading were synthesised using the sol-gel method at a *pH* of 0.4 and 1.5. The synthesised pure TiO_2 samples, alongside the commercial TiO_2 (Degussa® P25), were also doped with copper via the incipient wetness method. The low *pH* and the presence of copper inhibited the anatase-rutile transformation. Copper existed in Cu(I) and Cu(II) states in all the doped samples, with the Cu(I) to Cu(II) ratio intimately linked with the anatase to rutile ratio. The UPS data have shown the type II band offset between TiO_2 and CuO. The performance of the samples prepared was tested through the reduction of sodium bicarbonate-carbonate buffered at $pH > 8$. Commercial TiO_2 impregnated with Cu demonstrated the highest formate production rate of 173 $\mu mol \cdot g^{-1} \cdot h^{-1}$ at *pH* 11. This study demonstrated the synergetic effect of the anatase-rutile mixture of phases, the reaction *pH,* and the copper dopant in improving the photocatalytic activity of TiO_2.

1. Introduction

The continuous growth in world population and the high demand for energy and synthetic materials create great concerns towards the increase of CO_2 concentration in atmosphere due to the resulting emissions from the combustion of non-renewable fossil fuels. Every year, more research is being carried out exploring ways to control the atmospheric concentration of CO_2, ranging from carbon capture and storage to conversion into added value products [1,2]. The captured CO_2 is often stored underground, posing the risk of leakage, and the pumping and compression process is energy intensive, thus, a more sustainable solution is to convert the CO_2 into chemicals and fuel using renewable energy [3]. Thermochemical and electrochemical methods were reported to have been used in CO_2 conversion. In the former method, high amounts of energy are required to attain operation temperatures of 900 – 1000 °C due to unfavourable thermodynamics [1], while in the latter method, gas-liquid-solid mass transfer limitations are observed due to the low solubility of CO_2 in the aqueous electrolyte phase, thus limiting selectivity [2]. Therefore, there is the scope and need to develop novel, sustainable and more efficient technologies for CO_2 conversion and valorisation.

One promising alternative technology is photocatalysis, a process that harnesses light energy to activate a catalyst on which a redox reaction takes place. Photocatalytic CO_2 reduction is growing in popularity among researchers [4,5]. Aside from enabling production of chemicals and fuels through consumption of greenhouse gases, photocatalytic CO_2 reduction is highly advantageous over conventional conversion methods for it harnesses renewable solar energy, operates under mild operation conditions, does not require further thermal energy input [4] and has net zero emission of greenhouse gases [6]. Similar technology is already in use in environmental, energy production and pharmaceutical applications [7]. For the process to be effective, development of an efficient photocatalyst is essential.

Photocatalysts are usually semiconductors with a relatively low band gap energy, usually within the range of 1 – 4 eV [8], which enable the electron at the valence band to be excited to the conduction band when irradiated with a photon of ultraviolet (UV) or visible light, leaving an electron hole in the valence band [7]. For this to happen, the

Abbreviations: SG, sol-gel; IW, incipient wetness; H, high pH = 1.5; L, low pH = 0.4; A, anatase phase; R, rutile phase; PDAD, photodiode array detector.

* Corresponding author.
E-mail address: fernando.russo-abegao@newcastle.ac.uk (F.R. Abegão).

https://doi.org/10.1016/j.jcou.2023.102428
Received 18 October 2022; Received in revised form 19 January 2023; Accepted 7 February 2023
Available online 14 February 2023

illuminating photon energy irradiated must be greater than the band gap of the photocatalyst [9]. The basic properties of semiconductors, and their differences compared to metals and insulators can be understood by studying their band structure [10].

Photocatalytic CO_2 reduction involves multi-electron transfer leading to formation of a number of products, imposing challenges of low selectivity. Fig. 1 depicts a wide range of CO_2 reduction products reported in literature. The selectivity towards the desired product could be increased by selecting a photocatalyst with conduction potential close to the redox potential of the targeted products.

Despite advancement in the development of novel photocatalysts, titania (TiO_2) remains the most reported and studied material due to its favourable properties such as availability, low cost, high chemical stability [11] and low toxicity. TiO_2 occurs in 3 different crystal polymorphs at atmospheric pressure: anatase, rutile and brookite [7,12]. These phases exhibit different photocatalytic properties due to their difference crystal structures and orientation. The structure of the phases consists of TiO_6 octahedra, sharing 4 and 2 edges in anatase and rutile respectively. Table 1 summarises the properties of TiO_2 phases.

The most stable phase is rutile, while anatase and brookite are metastable and can easily be transformed to the stable rutile phase, subject to an increase in temperature or pressure [13], or through changes in *pH* [16], which makes control of these factors critical during catalyst synthesis to ensure the most appropriate phase is obtained. This phase transformation is also influenced by factors such as particle size, presence of dopants, synthesis method, annealing rate and morphology [7,13]. The anatase-rutile transformation takes place via bond breaking and recombination. Anatase is shown to have higher photocatalytic performance than rutile [17], even though rutile has a lower band gap energy. This has been attributed to a high efficiency of charge separation [18] and high density of superficial hydroxyl group [19] in the anatase compared to the rutile.

Different forms (*e.g.* crystals, nanoparticles, powder) of single or mixed phase TiO_2 can be obtained depending on the synthesis method used (Table 2), with each method having advantages and disadvantages. Amongst all methods, sol-gel methods stand out as these can easily be carried out without specialised equipment, at mild conditions, while still offering control on the properties of the materials produced. In sol-gel methods, aside from the calcination temperature, the *pH* of the synthesis medium determines the structure and phases present in the final TiO_2 photocatalyst. Under the condition of increased H^+ concentration, formation of the rutile phase is favoured while in the region of low H^+ concentration, anatase formation is favoured. Tryba, et al. [20] synthesised TiO_2 based photocatalysts at *pH* of 1.5 and 3. They reported that, under a *pH* of 1.5, the sample consisted of 20% rutile, against almost no rutile being present at *pH* of 3. Karami [21] similarly reported that anatase formation is favoured at *pH* of 3.

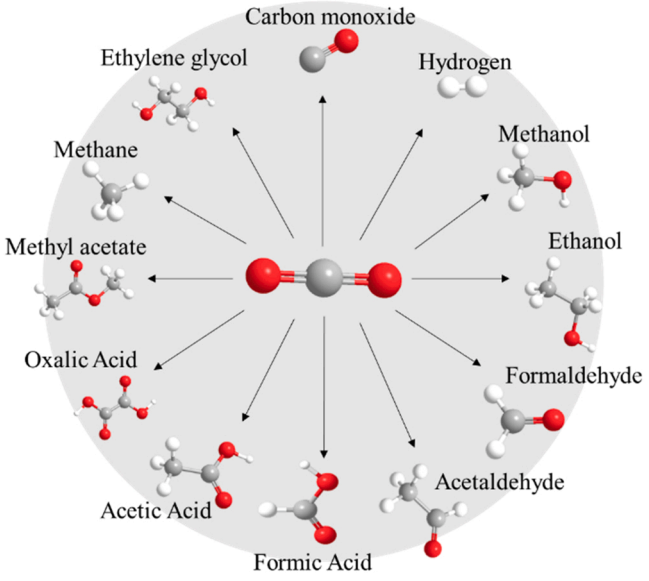

Fig. 1. Typical CO_2 reduction products reported in literature.

Table 1
Bulk properties of TiO_2 polymorphs. [13–15].

Property	Anatase	Rutile	Brookite
Crystal structure	Tetragonal	Tetragonal	Orthorhombic
Atoms per unit cell	4	2	8
Density, g cm^{-3}	3.83	4.24	4.17
Band gap, eV	3.26	3.05	
Refractive index	2.57	2.95	2.81

Table 2
Advantages and disadvantages of different TiO_2 synthesis methods.

Synthesis Method	Phases		Advantage	Disadvantage	Ref.
	Anatase	Rutile			
Precipitation	✓	✓	-Low temperature.	- Poor control of particle size. - Particle agglomeration.	[13]
Solvothermal/ Hydrothermal	✓	✓	- Easy control of surface properties. - Easy control of particles properties. - High purity.	- Long synthesis duration. - High cost of equipment.	[22]
Sol-gel	✓	✓	- Homogeneity. - Doping flexibility. - Low temperature.	- Decrease in surface area at calcination stage.	[13, 22]
Micro-emulsion	Amorphous			- Uncontrolled aggregation and flocculation.	[13, 23]
Combustion	✓		- Fine crystal with large surface area.		[13]
Chemical vapour deposition (CVD)	✓	✓	- Particles with large surface area.	- Difficult to control particle properties. - Capital and energy intensive.	[22]

Pure TiO_2 has low photocatalytic efficiency [2,9] due its high band gap as shown in Table 1. As a result, it typically operates within the UV spectrum and therefore it utilises a minimum amount of the total sunlight spectrum available [2]. It also offers low photocatalytic efficiency due to electron-hole recombination [24] and low reduction potential of its electrons in the conduction band. To overcome these limitations several strategies have been considered such as doping with metals, non-metals and co-metals, and photosensitisation through dye sensitisation, quantum dots and semiconductors coupling [2,5].

Doping is the process of adding impurities to a semiconductor aiming to modify its band structure [25] and is one of the most simple and cost effective catalyst modification processes to carry out. Dopants can either decrease the band gap energy, or promote/inhibit the anatase to rutile transformation by penetrating into the anatase lattice and changing the level of oxygen vacancies [7]. Non-metals, such as nitrogen [26,27], carbon [28] and metals (usually transition [29] and/or noble metals [30]) are widely used to minimize the effect of charge-carrier recombination by serving as either traps or sinks for charge carriers. The

elementary steps involve in a photocatalytic process are shown in Fig. 2.

Sangpour, et al. [31] compared the photocatalytic activity of TiO_2 doped with gold, silver and copper. Their result shows that the copper competes with the noble metals in enhancing the photocatalytic activity of TiO_2. Copper is one of the most extensively studied dopants used to improve the photocatalytic performance of TiO_2 [32–36]. Addition of Cu has been shown to inhibit anatase-rutile transformation during calcination [20]. Doping TiO_2 with Cu in the form of either CuO or Cu_2O has been reported to show enhanced photocatalytic performance for substrate degradation [37,38], hydrogen generation [39] and CO_2 photoreduction [40]. On doping TiO_2 with Cu, Tryba, et al. [20] reported enhanced light absorption with catalysts prepared at *pH* of 1.5 and calcined at 500 °C whereby rutile phase composition increased from 20% to around 75% with a reduction in band gap energy from 2.93 to 2.86 eV. There is a growing interest in using Cu dopants to explore its potential in addressing some of the limitations associated with TiO_2 [32, 41–43]. However, these studies focus on the study of influence of dopant loading [32,44,45]. There are however, limited systematic studies of different synthesis methods and the influence of Cu/TiO_2 synthesis conditions on TiO_2 phases and copper species distribution, alongside optimising testing conditions specifically for the reduction of dissolved CO_2.

The photocatalytic reduction of CO_2 is limited by poor solubility of CO_2 in water under acidic conditions at ambient temperature and atmospheric pressure. Its single electron reduction in water to a more active $^{\bullet}CO_2^-$ radical requires the standard reduction potential of 1.9 eV [46]. The solubility of CO_2 is improved by dissolution under pressure, or through increasing the *pH* of solution. CO_2 can be easily dissolved in a basic medium, usually using an aqueous solution of NaOH. Different forms of CO_2 ($H_2CO_3/HCO_3^-/CO_3^{2-}$) are formed depending on the *pH,* as shown in the reactions (1) and (2). Within the *pH* ranges of 4 – 8 and 8 – 11, the solution contains CO_2/HCO_3^- and HCO_3^-/CO_3^{2-} forms respectively. The Pourbaix diagram reported by Reda, et al. [47] shows which forms are most stable thermodynamically at different *pH* and reduction potential to formate or formic acid. A detailed mechanistic scheme of the reduction of different forms of CO_2 was proposed by Karamian, et al. [48].

$$CO_2 + NaOH_{(aq)} \xrightarrow{pH=8.4} Na^+_{(aq)} + HCO_{3\,(aq)}^- \quad (1)$$

$$HCO_{3\,(aq)}^- + NaOH_{(aq)} \xrightarrow{pH>11} Na^+_{(aq)} + CO_{3\,(aq)}^{2-} + H_2O_{(l)} \quad (2)$$

This study covers the systematic investigation into the effect of *pH* in enhancing the photocatalytic performance of TiO_2 for CO_2 reduction, both during catalyst synthesis and during reaction. TiO_2 and Cu/TiO_2 samples were successfully synthesised using simple sol-gel and incipient wetness methods. The effects of *pH* during synthesis on the physiochemical properties of the photocatalyst samples and on their performance for photocatalytic reduction of sodium bicarbonate/carbonate to formate were investigated. Specifically, the influence of the *pH* used during the sol-gel synthesis of TiO_2 on the composition of TiO_2 phases, Cu speciation, band gap energy and band offset between Cu and TiO_2 were studied. The effect of the *pH* of the reaction medium was also examined. Copper dopant was selected due to its availability, low cost [49], exhibition of multiple oxidation states [50] and its ability to readily substitute Ti^{+4} of TiO_2 network [33]. P25 is a commercial TiO_2 product prepared by pyrogenic method and commonly used as benchmark. The detailed procedure of this method is not available. Although the P25 was used for benchmarking in this work, the use of extensively studied sol-gel method was chosen to understand the impact of different synthesis condition on the photocatalyst properties and activity to allow further improvements, and also to match the performance of P25 using a more readily available synthesis method.

2. Methodology

2.1. Photocatalyst preparation

2.1.1. Preparation of TiO_2

Two 10 g TiO_2 samples were prepared using sol-gel method at two different *pH* values. Titanium butoxide ($C_{16}H_{36}O_4Ti$, 99 +%, Alfa Aesar), methanol (CH_3OH, ≥ 99.9%, Fisher Scientific,) and nitric acid (HNO_3, 70%, Fisher Scientific) were used at a mole ratio of 1:10:30 as precursor, solvent and catalyst, for the hydrolysis and condensation reactions taking place during the sol-gel synthesis respectively. The procedure involved the dissolution of 36 ml titanium butoxide in 42 ml of methanol under continuous stirring at 300 rpm for 15 min, followed by the dropwise addition of nitric acid solution prepared by adding 1.58 ml and 0.12 ml of nitric acid into 60 ml of DI water, corresponding to a *pH* of 0.4 and 1.5 respectively. These *pH* values were determined based on a review of previous literature where the effect of *pH* on the kinetics of hydrolysis and condensation reaction during sol-gel synthesis is described [7,51–54]. After the addition of nitric acid, the mixture was covered with parafilm whilst being stirred for 30 min. The mixture was

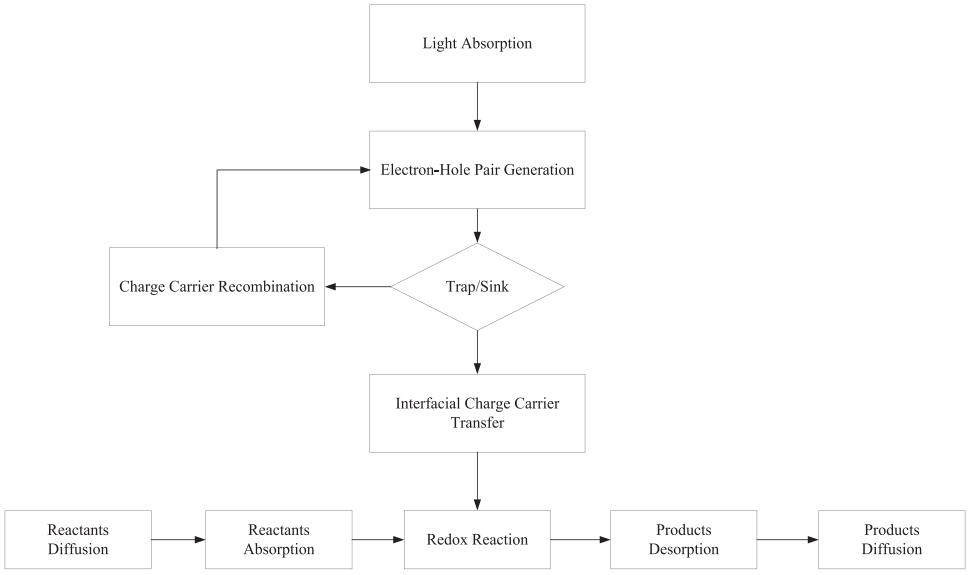

Fig. 2. Elementary steps in photocatalysis.

then allowed to age for 24 h before drying at 90 °C for 24 h followed by calcination at 500 °C. The calculation furnace temperature was ramped at 5 °C min^{-1} up to 500 °C, kept at 500 °C for 2 h and then let to cool naturally to 50 °C at which point the samples were removed. The samples prepared at 0.4 and 1.5 *pH* were labelled SGL-TiO_2 and SGH-TiO_2 respectively. Commercial TiO_2 (Aeroxide ® P25, Acros Organics) was used to benchmark the in-house TiO_2. The final samples were ground in ethanol (Fisher Scientific 99.8%) using a Retsch planetary ball mill (PM 100) equipped with a 125 ml fused zirconia grinding jar and Ø 10 mm balls. The mill was operated at 300 rpm for 90 min

2.1.2. Preparation of copper-doped TiO_2

A 5 wt% loading of Cu was selected and fixed in this study as it was sufficient to impart an influence on the catalytic activity and be detected during characterisation, enabling analysis of its influence on the optical properties of the TiO_2 without masking the effects of TiO_2. Sol-gel and incipient wetness methods were used to prepare 10 g of 5 wt% copper-doped TiO_2 photocatalyst samples, in both cases using copper nitrate trihydrate ($Cu(NO_3)_2{\cdot}3\ H_2O$, 99%, Fisher scientific) as doping agent precursor.

For the sol-gel method, a similar procedure as described in Section 2.1.1 was implemented, with addition of 1.71 g copper nitrate trihydrate into the HNO_3 solution before mixing with the titanium butoxide and methanol. The samples prepared at *pH* 0.4 and 1.5 were labelled as SGL-Cu/TiO_2 and SGH-Cu/TiO_2.

For the incipient wetness method, both the commercial and the TiO_2 prepared in Section 2.1.1 were doped with copper via the incipient wetness method. For this, 1.9 g of copper nitrate trihydrate was dissolved in 2.76 ml of water. The solution was then mixed with 9.5 g of TiO_2. The volume of the solution was just sufficient to fill the pore volume of the TiO_2. The pore volume at 'incipient wetness' was measured by gravimetric dosing of water onto the TiO_2 powder with manual mixing, until the powder lost the free flow characteristics. Assuming the density of water is 1 g/ml, the volume of the pore was estimated by subtracting the final weight of the impregnated powder from the initial weight of the loose powder before impregnation.

All of the photocatalyst samples were oven dried at 90 °C and calcined in air at temperature ramp of 5 °C/min up to 500 °C with a dwell time of 2 h. The final catalyst samples, labelled as IW-Cu/P25, IW-Cu/SGL-TiO_2 and IW-Cu/SGH-TiO_2, after drying and calcination were ground to a powder using a mortar and pestle. Table 3 summarises the methods and conditions under which all the photocatalyst samples were prepared.

2.2. Photocatalyst characterisation

The X-ray diffraction pattern of the samples were measured using a PANalytical X'Pert Pro Multipurpose Diffractometer (MPD) in the range of 2θ° from 10° to 110° at 0.033° step and 750 s per step. 40 kV generator voltage and 40 mA tube current with Cu Kα (λ = 1.541874 Å)

Table 3
Photocatalyst samples prepared.

Catalyst Samples	*pH* During Sol-Gel Step*	Synthesis Method
TiO_2 (P25)		Pyrogenic
SGL-TiO_2	0.4 (L)	Sol-gel (SG)
SGH-TiO_2	1.5 (H)	Sol-gel (SG)
SGL-Cu/TiO_2	0.4 (L)	Sol-gel (SG)
SGH-Cu/TiO_2	1.5 (H)	Sol-gel (SG)
IW-Cu/P25		Incipient wetness (IW)
IW-Cu/SGL-TiO_2	0.4* (L)	Incipient wetness (IW)
IW-Cu/SGH-TiO_2	1.5* (H)	Incipient wetness (IW)

* The *pH* for these samples refers to the *pH* of the nitric acid solution used to prepare the TiO_2 material during the sol-gel procedure. L refers to a "low" *pH* value of 0.4, and H refers to a "high" *pH* value of 1.5.

as anode material were used. The Rietveld refinements were performed using PANalytical HighScore Plus. Semi-quantitative analysis built in the HighScore Plus working on the basis of the reference intensity ratio values was used to estimate the mass fraction of the identified phases.

Scanning Electron Microscopy (SEM) was conducted using XL30 ESEM-FEG to understand the surface morphology of the catalyst samples. UV–vis diffuse reflectance spectroscopy was used for band gap measurement by measuring the reflectance using a Flame S UV–vis spectrometer from Ocean Optics equipped with a bifurcated reflectance optical fibre (QR230–7-XSR) and a high power Deuterium and Tungsten Halogen light source (DH-MINI). A PTFE reflectance standard was used to acquire a reference spectrum.

XPS data was acquired using a Kratos Axis SUPRA using monochromated Al kα (1486.69 eV) X-rays at 15 mA emission and 12 kV HT (180 W) and a spot size/analysis area of 700 × 300 μm. The instrument was calibrated to gold metal Au 4 f (83.95 eV) and dispersion adjusted give a BE of 932.6 eV for the Cu $2p_{3/2}$ line of metallic copper. Ag $3d_{5/2}$ line FWHM at 10 eV pass energy was 0.544 eV. Source resolution for monochromatic Al Kα X-rays is ~0.3 eV. The instrumental resolution was determined to be 0.29 eV at 10 eV pass energy using the Fermi edge of the valence band for metallic silver. Resolution with charge compensation system on < 1.33 eV FWHM on PTFE. High resolution spectra were obtained using a pass energy of 20 eV, step size of 0.1 eV and sweep time of 60 s, resulting in a line width of 0.696 eV for Au $4f_{7/2}$. Survey spectra were obtained using a pass energy of 160 eV. Charge neutralisation was achieved using an electron flood gun with filament current = 0.38 A, charge balance = 2 V, filament bias = 4.2 V. Successful neutralisation was adjudged by analysing the C 1 s region wherein a sharp peak with no lower BE structure was obtained. Spectra have been charge corrected to the main line of the carbon 1 *s* spectrum (adventitious carbon) set to 284.8 eV. All data was recorded at a base pressure of below 9×10^{-9} Torr and a room temperature of 294 K. UPS data was performed using a He(I) (21.22 eV) lamp. Data was analysed using CasaXPS v2.3.19PR1.0. Peaks were fitted with a Shirley background prior to component analysis.

2.3. Photocatalytic CO_2 reduction

The prepared photocatalyst samples alongside P25, used as a benchmark, were tested for CO_2 reduction in basic medium. The photocatalytic activity experiments were conducted in an Immersion Well Photochemical Reactor, Model RQ125, with 250 ml volume capacity. The reactor was equipped with a 125 W medium pressure mercury lamp emitting predominantly between 365 and 366 nm radiation, with smaller amounts also in the ultraviolet region at 280, 289, 292, 296, 302, 313 and 334 nm, and a significant amount of radiation produced in the visible region at 405–408, 436, 491, 546–550 and 577–579 nm. The light source was positioned at the centre of the reactor, surrounded by a quartz jacket (immersion well) through which cooling deionised water was circulated to cool the light source and control the reaction temperature. The deionised water is generally transparent to visible light but can absorb some UV radiation, particularly in the short-wavelength UV-C range (200–280 nm, i.e. 6.9–4.43 eV). However, it can also transmit UV radiation at longer wavelengths (280–400 nm, i.e. 4.43–3.1 eV) [55]. The spectral range of the light source used was measured using an Ocean Optics Flame S UV–vis spectrometer coupled with a QP230–2-XSR solarisation-resistant optical fibre on the outside of the water jacket, i.e. in the same space occupied by the reaction medium. It was found that the light source emitted radiation with energy between 270 and 506 nm, (i.e. 2.45–4.6 eV) approximately (cf. Supplementary Information S1). UV-A/B radiation intensity (280–400 nm, i.e. 4.43–3.1 eV) was measured using a General UV513AB light meter and found to be in the region of 40 mW/cm^2 in the region of maximum intensity demonstrating a high radiation intensity was still available despite the water jacket (cf. Supplementary Information S2). All experiments were performed in the same conditions and using the same set

up, thus all results are comparable.

The immersion well is then inserted into an external vessel (reaction flask) to create an annular space (ID of the reaction flask 65 mm and OD of the immersion well 58 mm, corresponding to an optical path of 3.5 mm) where the catalyst slurry was mixed and irradiated. Mixing was achieved with a magnetic stirrer positioned under the reactor. The reactor was isolated in a safety cabinet equipped with a safety switch to prevent exposure to hazardous UV radiation before turning on the UV light source. The experimental set up is shown in Fig. 3.

Sodium bicarbonate/carbonate were used as these are commonly the product of absorption of carbon dioxide in sodium hydroxide solutions. The reactor was operated under batch mode to photocatalytically reduce the bicarbonate/carbonate to formate. To study the effect of *pH*, different carbonate/bicarbonate buffers were tested on photocatalyst samples prepared.

250 ml of 0.1 M aqueous solutions for each of sodium bicarbonate (Na_2CO_3, ≥99.95%, Acros organics, *pH* 8.34) and carbonate ($NaHCO_3$, ≥99.5%, Acros organics, *pH* 11.72) solutions as well as the mixture of $NaHCO_3/Na_2CO_3$ at the ratio of 0.9, 0.5 and 0.1, corresponding to *pH* values 9.16, 10.09, and 11 were prepared. The reaction mixture was prepared by adding 0.1 g of photocatalyst to 200 ml of the buffer solution contained in the 250 ml photoreactor. The reaction mixture was kept under constant magnetic stirring at 1000 rpm to prevent catalyst sedimentation and to provide uniform distribution of catalyst particles within the reaction volume. The temperature of the photoreactor setup was kept at 40 °C by water recirculating through a chiller. The reactor was then sealed using a stopcock. The mixture was irradiated for 5 h and 8 ml liquid samples were taken through the sampling port at hourly intervals and filtered through 0.45 μm membrane filters. The samples were analysed on a Perkin Elmer Flexar HPLC system, equipped with an Ultra Aqueous C18 150 mm × 4.6 mm column, photodiode array detector (PDAD) at the analytical wavelength of 230 nm.

3. Results and discussion

3.1. Photocatalyst characterisation

3.1.1. SEM imaging

The SEM images of the samples at 10,000 × magnification is presented in Fig. 4. The image revealed that the samples prepared have different grain sizes and surface morphology. P25 appeared more homogeneous with more finer grains than the samples prepared via sol-gel method, as is characteristic of pyrogenic aerosol preparation methods [56]. Samples prepared via sol-gel method at *pH* 1.5 have somewhat finer grains with relatively regular shape compared to samples prepared at *pH* 0.4. In the hydrolysis stage at *pH* 0.4, a gel is formed, which upon calcination would easily fuse to form the irregular shape and 'glass-like grains observed in the SGL-TiO_2, where rutile composition is high. In contrast, at *pH* 1.5, a sol is formed, which upon calcination would form a more regular shape grains as is observed in the SGH-TiO_2 sample of predominantly anatase phase. Challagulla, et al. [57] have shown the dependence of morphology of TiO_2 relative to its phase composition.

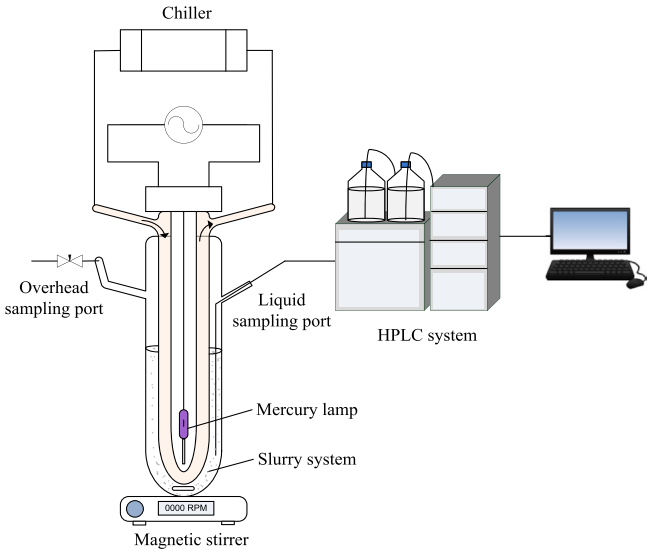

Fig. 3. Schematic view of the experimental set up.

3.1.2. XRD analysis

The X-ray diffraction patterns for all the 8 samples are shown in Fig. 5. The patterns indicate that commercial P25 and the SGL-TiO_2 sample synthesised at *pH* of 0.4 contained mixed anatase and rutile phases. As shown in Table 4, for the bare TiO_2 samples, the commercial P25 has the highest anatase to rutile phase (A/R) of the 4 compared to the SGL-TiO_2 with an A/R of 0.6. The anatase to rutile ratio of the commercial TiO_2 (P25) is within the range of values (2.3 – 4) reported by Ohtani, et al. [17]. However, the SGH-TiO_2, sample prepared at *pH* of 1.5 contained predominantly the anatase phase. Additionally, traces of a brookite pattern assigned to the (121) plane was also observed in all the samples. It is often observed that, under highly acidic conditions, the rate of hydrolysis (reaction 3) is higher than the rate of condensation (reaction 4). This leads to intramolecular oxolation of the hydrolysed titanium precursor and linear rutile growth takes place along the equatorial plane of the hydrolysed sample. On the contrary, a lower acidity accelerates the condensation reaction more than the hydrolysis reaction, and deoxolation takes place, with growth proceeding along the apical direction leading to formation of skewed chains of anatase structure [20].

$$TiO_4(C_4H_9)_4 \xrightarrow{\text{Hydrolysis}} Ti(OH)_4 + 4C_4H_9OH \quad (3)$$

$$nTi(OH)_4 \xrightarrow{\text{Condensation}} nTiO_2 + 2nH_2O \quad (4)$$

The average crystallite sizes of the samples, calculated using Scherrer's Eq. (5), are shown in Table 4.

$$D = K\lambda/\beta Cos\theta \quad (5)$$

where D is the crystallite size in nm, K is the shape factor (K=0.9 for spherical crystallites), λ is the wavelength for copper kα_1 radiation in Å (λ = 1.541874 Å), β is the full width at half maximum for the peak being measured, and θ is half of Bragg's angle in radians. The average anatase crystallite sizes at (101), (004), (200) and (211) planes for SGL-TiO_2 and SGH-TiO_2 samples were 18.9 ± 0.62 nm and 15.5 ± 1.37 nm respectively, while the average rutile crystallite size at (110), (101), (111) and (310) for SGL-TiO_2 was 32.5 ± 1.71 nm.

There are conflicting conclusions in the literature regarding the influence of crystallite size on the photocatalytic performance of a photocatalyst. Generally, for a single-phase crystal, there is strong evidence that increasing crystallite size enhances photocatalytic activity up to a certain optimum range. For an anatase phase within the range of 6.6 – 26.6 nm, Wang, et al. [58] reported an increase in photocatalytic performance for phenol degradation with increasing crystallite size. Furthermore, Kočí, et al. [59] reported that for photocatalytic CO_2 reduction within the range of 4.5–29 nm, the highest yield of methane and methanol was recorded at 14 nm. Smaller crystals are subject to a rapid agglomeration, thereby reducing their surface area.

CuO XRD diffraction peak was not detected in samples prepared via sol-gel method suggesting a high dispersion of the Cu and incorporated into the network of the TiO_2 [60]. For the sol-gel samples where the Cu doping was carried out as part of the sol-gel procedure, introduction of a Cu dopant at *pH* = 0.4 (SGL-Cu/TiO_2) inhibited anatase to rutile transformation, causing an increase in anatase to rutile ratio from 0.6 to 3.8, likely due to incorporation of Cu into the TiO_2 network [61]. The inhibition of anatase-rutile transformation on doping with Cu were

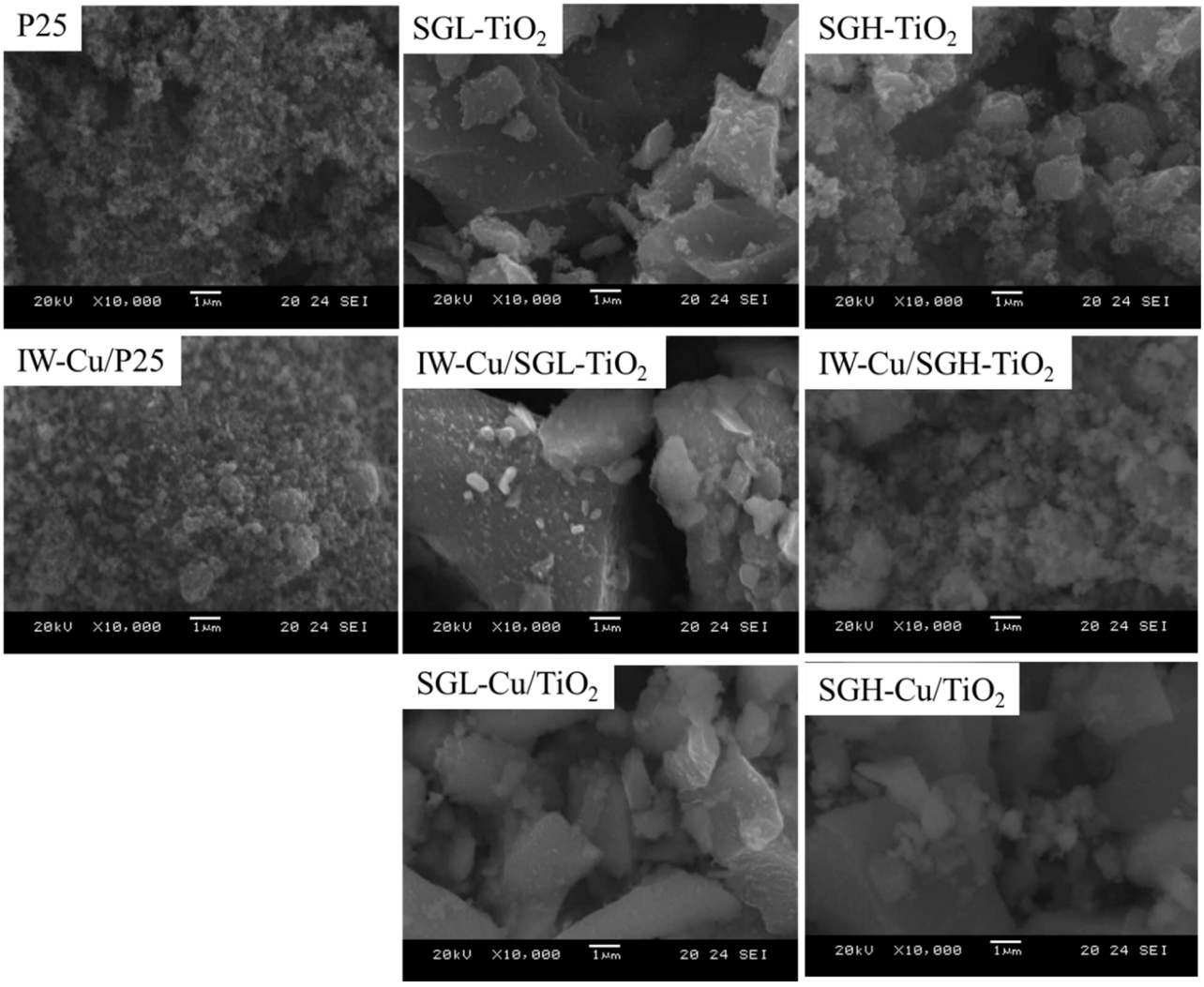

Fig. 4. SEM images of the prepared samples.

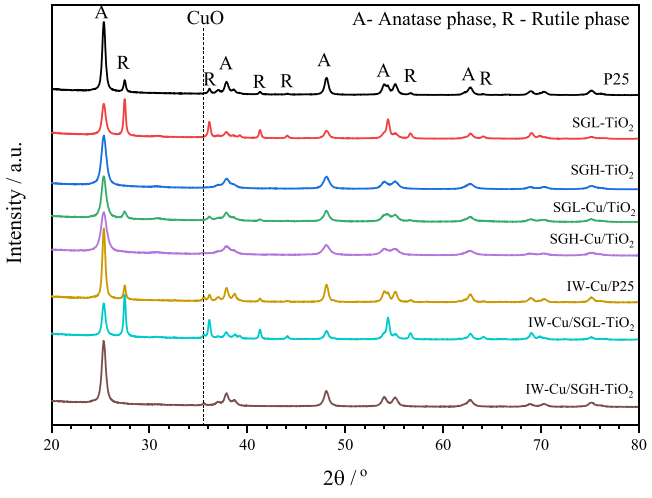

Fig. 5. X-ray diffraction pattern of TiO_2 based photocatalysts prepared at different *pH*.

previously reported by Byrne, et al. [62]. This was accompanied by a decrease in rutile crystallite size from 32.5 nm to 19.7 nm. For the TiO_2 samples doped with Cu at *pH* 1.5 (SGH-Cu/TiO_2), the anatase phase was maintained with no significant change in the crystallite size (15.5 ± 1.37 nm and 13.9 ± 1.7 nm).

Phase transformation and crystallite size remained unchanged, within the margin of measurement error, for both in-house and commercial TiO_2 samples impregnated with Cu. The diffraction peak observed in all Cu impregnated samples at $2\theta = 35.5°$ corresponds to

Table 4
Phase composition, crystallite size and band gap energy of the prepared photocatalyst samples.

Catalyst samples	Phase (composition) / wt%	Crystallite size / nm	Band gap energy / eV	
			Direct	Indirect
TiO_2 (P25)	A (80) / R (20)	21.9 / 35.5	3.72	3.24
SGL-TiO_2	A (39) / R (61)	18.9 / 32.5	3.29	2.96
SGH-TiO_2	A (100)	15.5	3.74	3.25
SGL-Cu/TiO_2	A (79) / R (21)	17.6 / 19.7	3.29	2.61
SGH-Cu/TiO_2	A (100)	13.9	3.49	2.93
IW-Cu/P25	A (73) / R (20) / CuO (8)	22.4 / 35.6 / 35.1	3.69	3.08
IW-Cu/SGL-TiO_2	A (34) / R (61) / CuO (5)	20.3 / 32.4 / 51.4	3.12	2.22
IW-Cu/SGH-TiO_2	A (92) / CuO (8)	16.0 / 30.1	3.63	3.06

– A – Anatase phase, R – Rutile phase

footprints of CuO, suggesting a higher level of segregation between the copper and titanium oxide phases when incipient wetness is used as a doping technique.

3.1.3. Band gap measurements

It has been shown that TiO_2 has direct and indirect electronic transitions, depending on its phase composition [63]. The band gap energy was estimated using the Tauc expression [64]:

$$(\alpha h\upsilon) = A\left(h\upsilon - E_g\right)^n \quad (6)$$

where A is a constant, E_g is the band gap energy in eV, α is the absorption coefficient, $h\upsilon$ is the energy of excitation in eV, n indicates different types of transition ($n = ½$ and 2 for direct and indirect transitions respectively).

The measured reflectance spectra are shown in Fig. 6. The absorption coefficient was determined from the reflectance data obtained using the expression:

$$F(R_\infty) = \frac{(1-R_\infty)^2}{2R_\infty} = \frac{\alpha}{S} \quad (7)$$

where R_∞ is the absolute reflectance, S is the scattering coefficient, independent of the wavelength.

The associated functions for determination of the band gap energies are presented in Fig. 7. The values of the band gap energies shown in Table 4 were determined by linear regression through the linear region of the $(\alpha h\upsilon)^2$ (Fig. 7a) and $(\alpha h\upsilon)^{1/2}$ (Fig. 7b) versus $h\upsilon$ functions for direct and indirect transition, respectively, followed by extrapolation of the fitted lines to the points of intersection with the $h\upsilon$ axis.

From the results shown in Table 4, it is possible to see that the direct and indirect band gap energies of SGL-TiO_2 (3.29 eV and 2.96 eV) are lower than those of P25 (3.72 eV and 3.24 eV) and SGH-TiO_2 (3.74 eV and 3.25 eV). The photocatalyst band gaps were all ≤ 3.74 eV (spectral position shown in S1), confirming that the light obtained after passing the quartz-water jacket still has capacity to excite the samples tested in this study. The lower band gap of SGL-TiO_2 is related to its high composition of the rutile phase with an inherently lower band gap energy compared to the anatase phase. As shown in the Table 1, the band gap of the anatase phase, which almost corresponds to the indirect band gap energy of 3.25 eV for SGH-TiO_2, is higher than that of the rutile phase.

The direct band gap energy of the sample doped with Cu via sol-gel method at *pH* 0.4 (SGL-Cu/TiO_2) has not changed despite addition of the dopant due to an increase in anatase phase. However, the indirect band gap energy has shown a decrease by 0.35 eV upon doping with Cu. This suggests that the anatase phase has an indirect band transition as confirmed by the density of states profile of pure anatase [63]. The effect of Cu in terms of the direct and indirect band gap energy reduction by 0.25 eV and 0.32 eV respectively has been exhibited in samples doped with Cu via sol-gel method at *pH* of 1.5 with pure anatase (SGH-Cu/-TiO_2). A similar effect has been shown by all of the TiO_2 samples impregnated with Cu. We can therefore surmise that the reduction of band gap energy is due to the addition of Cu, rather than a changing crystal phase.

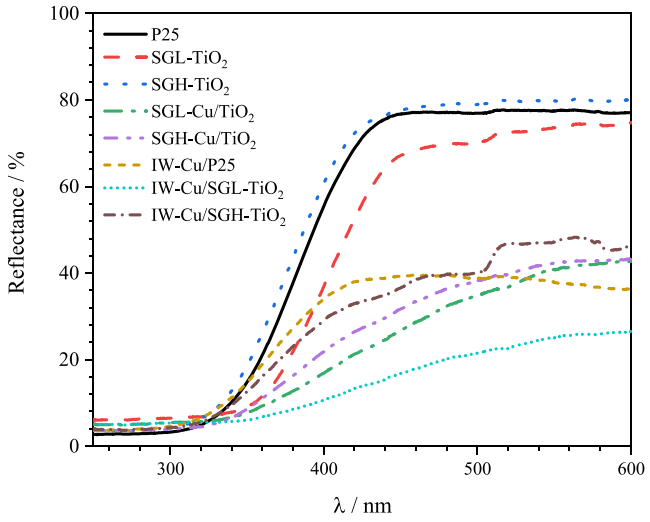

Fig. 6. UV–vis diffuse reflectance spectra of the prepared samples.

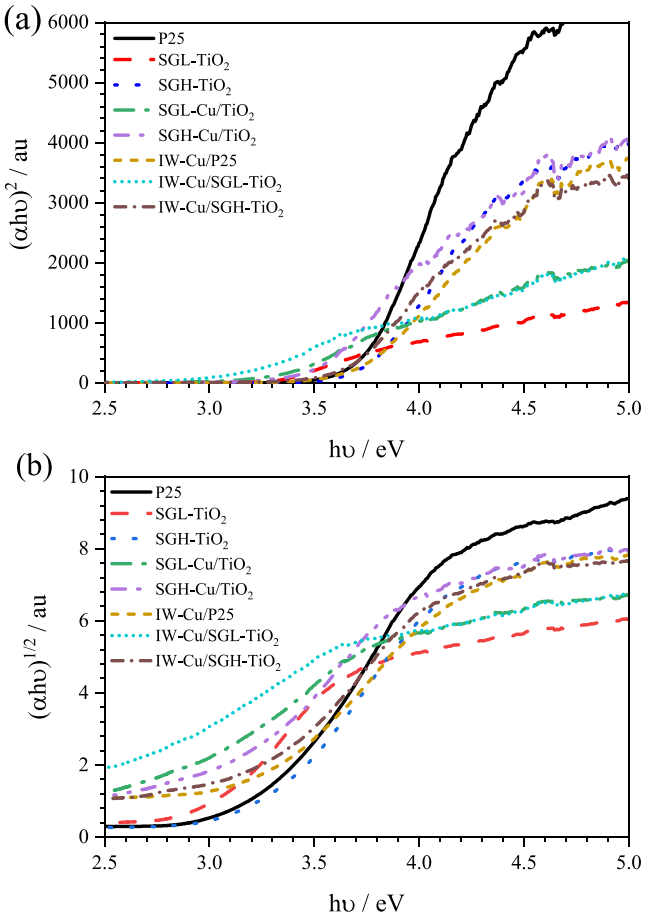

Fig. 7. Tauc plot of the (a) direct and (b) indirect transitions for the prepared photocatalyst samples.

The band gap energy is also influenced by crystallite size as shown using quantum confinement, which demonstrates that the band gap energy can be tailored by tuning the size and shape of a single phase material [65]. The crystallite size in turn was shown to be directly influenced by doping and synthesis conditions. For the samples prepared at *pH* 1.5 by both methods (SGH-Cu/TiO_2 and IW-Cu/SGH-TiO_2), there is no significant change in the crystallite size, thus the overlap of the discrete energy level of the Cu dopant with TiO_2 played a key role in reducing their band gaps. Comparing these two samples, doping via the sol-gel method produced a sample (SGH-Cu/TiO_2) with a lower direct and indirect band gap energy (3.49 eV and 2.93 eV) than that prepared via the incipient wetness method (IW-Cu/SGH-TiO_2), which had a direct and indirect band gap energy of 3.63 eV and 3.06 eV respectively. This was presumably due to the high dispersion of the dopant in SGH-Cu/TiO_2.

For samples with multiphase composition, the band gap energy is compounded by the optical properties of the individual phases. In addition to the presence of the Cu dopant, the decrease in the crystallite size of rutile phase from 32.5 nm to 19.7 nm is another potential reason

why the indirect band gap energy of SGL-Cu/TiO_2 decreases from 2.96 eV to 2.61 eV. In this sample, it is likely that the inhibition of anatase to rutile transformation overshadowed the role of Cu in decreasing the band gap energy. Therefore, it was clearly shown that the function of the dopant was to shift the absorption spectrum to regions with lower energy, expanding the amount of usable light from the UV into the visible range. In addition to the reduction in the band gap that contributed to the improved light efficiency of the photocatalyst, it is also expected that the dopant may act by way of an electron trap as demonstrated by Li, et al. [66], adding to the total photocatalytic efficiency.

3.1.4. XPS/UPS analysis

X-ray and ultraviolet photoelectron spectroscopies (XPS/UPS) were conducted to understand the chemical state of the copper species and establish the band edge position of the prepared samples. The high-resolution XPS spectra in the region of Ti 2p are shown in Fig. 8. In the spectra, only Ti(IV) was detected and there were no noticeable changes in the chemical state of titanium after doping with Cu.

While Cu(II) may be readily identified by XPS due to significant final-state satellite features, Cu(I) and Cu(0)are more difficult to distinguish using only the Cu 2p peaks due to low energy separations. The Cu LMM Auger, however, may be used to identify the nature of the emitting core-atom, and the representative Cu 2p and Cu LMM auger spectra for SGL-Cu/TiO_2 and SGH-Cu/TiO_2, indicating the deconvolution profile and differences in auger spectra, may be found in Fig. 9. Despite the presence of the Ti 2 s peak at 921.7 eV alongside the ligand-to-metal charge transfer (LMCT) shake-up at 909 eV, which complicated the identification of the copper peaks, quantification was still possible via background removal of the contributing Ti signal from the unmodified parent titania spectra. It is clear from the auger spectra (fit via linear combination fitting of Cu(I) and Cu(II) auger lineshapes from known standards) that there is no observable Cu(0) peaks within the dataset and hence the materials must comprise solely Cu(I) and Cu(II).

The relative percentages of Ti, O, and Cu were quantified and presented in the Supplementary Information S3. The initial ratio of copper to titanium (Cu:Ti) introduced during synthesis was 0.066. Analysis of the XPS data revealed that the final Cu:Ti ratios in the samples SGL-Cu/TiO_2, IW-Cu/P25 and IW-Cu/SGL-TiO_2 were greater than the ratio introduced, with values of 0.125, 0.139, and 0.171 respectively. In contrast, the samples SGH-Cu/TiO_2 and IW-Cu/SGH-TiO_2, which had final Cu:Ti ratios that were relatively close to the amount introduced (0.076 and 0.088, respectively). The high surface copper content in SGL-Cu/TiO_2, IW-Cu/P25 and IW-Cu/SGL-TiO_2 is attributed to the presence of a mixture of anatase and rutile phases. This is because anatase and rutile have different crystal structures, with rutile phase exhibiting a higher surface free energy compared to the anatase phase. As a result, defect sites are likely to form on the surface of the rutile phase [12]. The existence of these defect sites on the rutile surface provides binding sites for copper atoms.

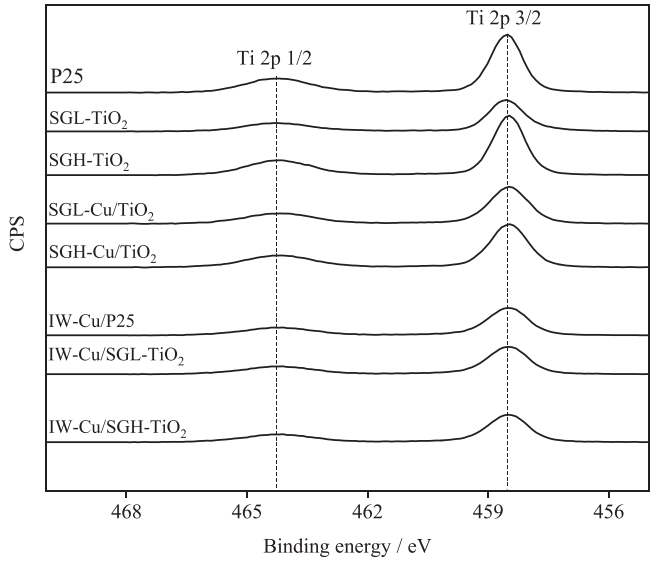

Fig. 8. High resolution XPS spectra of in the region of Ti 2p.

The atomic ratios of Cu(II) and Cu(I) extracted from the Cu 2p and Cu LMM Auger spectra are shown in Fig. 10 for all the Cu doped samples. We observe that, regardless of the synthesis method employed, all samples contain Cu(II) and Cu(I) in varying amounts. However, it is apparent that both for Cu-doped P25 (IW-P25) and for the Cu-doped titania samples synthesised at low *pH* during the sol-gel (SGL-Cu/TiO_2) and incipient wetness (IW-Cu/SGL-TiO_2) steps, we produce a high Cu(II) to Cu(I) ratio. Under the condition of the low *pH*, the ratio of Cu (II) to Cu(I) in the sol-gel sample (SGL-Cu/TiO_2) is almost double that of the sol-gel samples under the condition of high *pH* (SGH-Cu/TiO_2). In contrast, for the samples synthesised with a high *pH* during the sol-gel step, the ratio of Cu(II) to Cu(I) is much more comparable, with the Cu(I) content appearing to be the dominant phase in the SGH-Cu/TiO_2 and IW-Cu/SGH-TiO_2 samples.

The data seem to reveal that the synthesis *pH* not only determines phase composition as shown by the XRD data, but also determines the distribution of Cu(I) and Cu(II). The samples that only had anatase have similar amounts of Cu(I) and Cu(II), while samples that also had rutile have much higher amount of Cu(II) than Cu(I). The copper species distribution is shown to be controlled by both *pH* [67] and thermal treatment [68]. These parameters simultaneously influence the phase distribution of TiO_2. The distribution of copper species in this study can be explained by the fact that in acidic medium, formation of Cu(I) is favoured [69]. The Cu(I) in the SGH-Cu/TiO_2 sample is thermally more stable than the Cu(I) in the SGL-Cu/TiO_2 due to its high anatase content [70]. Anatase has high oxygen vacancies which act as electron accepters and promote the reduction of Cu(II) to Cu(I) by providing more electrons. This can help to stabilise the Cu(I) species, making it less likely to oxidise back to Cu(II) under thermal treatment [71].

The surface distribution of copper was investigated using energy dispersive X-ray (EDX) analysis. The result from the two-point analysis of only IW-Cu/P25 and SGL-Cu/TiO_2 samples (cf. Supplementary Information S4) revealed the presence of copper on the surface of these samples, which is in agreement with the XPS results. The EDX results revealed that the copper on the surface of SGL-Cu/TiO_2 relatively consistent across the two points analysed, indicating a relatively homogeneous distribution of copper on the surface, which is consistent with the samples being prepared via the sol-gel method. In contrast, the IW-Cu/P25 sample showed a significant variation in copper content between the two points on the surface, indicating a more heterogeneous distribution of copper, typically observed in samples where doping was deposited via the incipient wetness method.

The valence band minimum (E_{VBM}) was determined for TiO_2 samples via UPS spectroscopy. Fig. 11 shows the conduction band minimum (E_{CBM}) estimated from the E_{VBM} and from the band gap energies of the samples measured by UV-Vis Diffusive Reflectance Spectroscopy (cf. Table 4).

The reduction potential determines the tendency of chemical species to get reduced. For a chemical species to undergo reduction, its reduction potential must be higher than the reduction potential of the conduction band of the photocatalyst being used. In essence, the band edge position dictates if the photocatalytic reduction is thermodynamically favourable or not. The results shown in Fig. 11 seem to indicate that the reduction potential for the conduction band edge of the pure TiO_2 samples is within the range of the reduction potential for the bicarbonate and carbonate reduction pairs to formate (−0.35 V to −0.90 V) [47]. Therefore, kinetic limitations aside, all three TiO_2 catalysts should be good candidates to drive the reduction reaction of bicarbonate to formate forwards, but less so when it comes to directing the reduction of

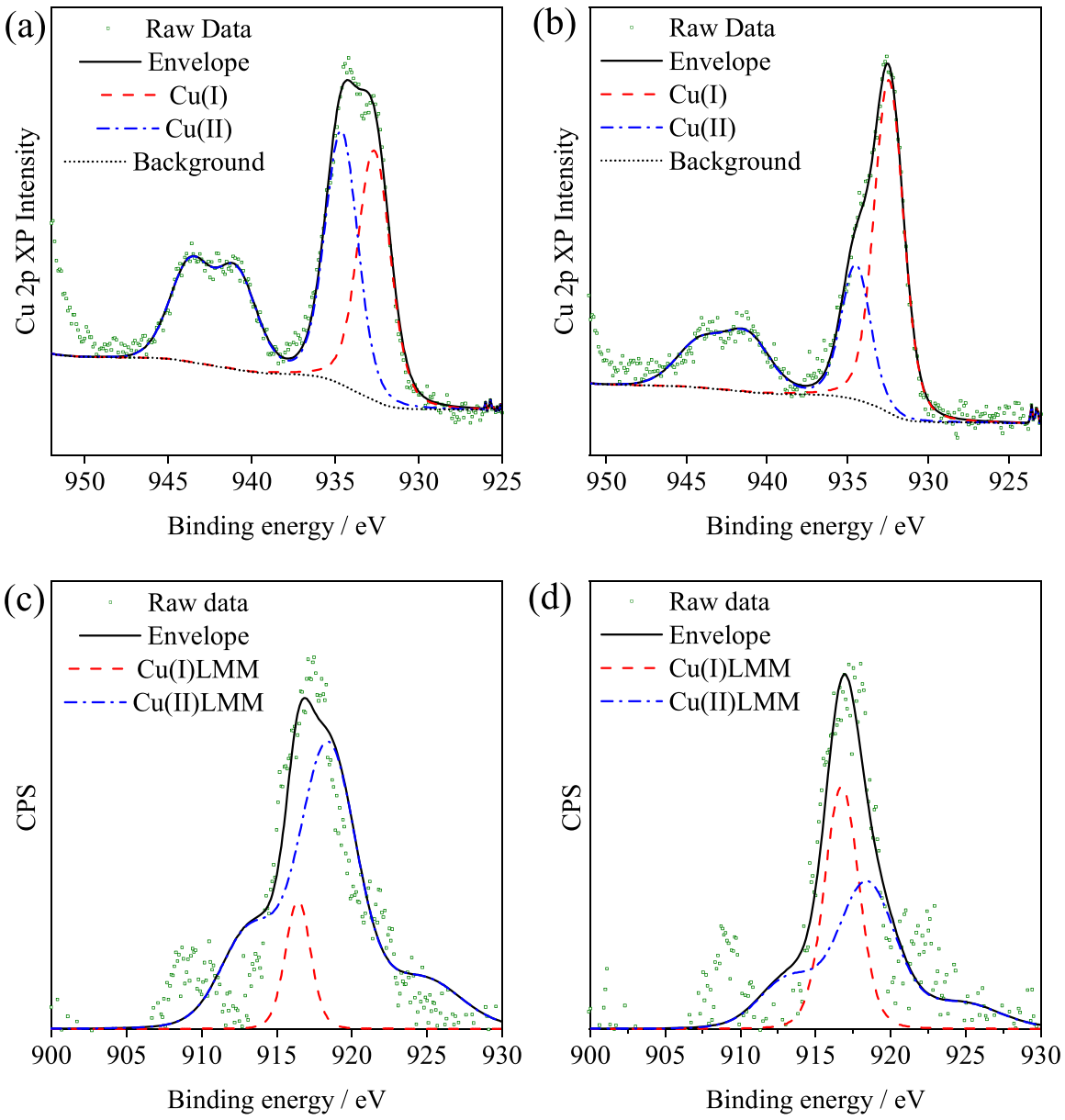

Fig. 9. Cu 2p photoemission spectra for (a) SGL-Cu/TiO_2 and (b) SGH-Cu/TiO_2, and deconvoluted Cu LMM auger emission spectra for (c) SGL-Cu/TiO_2 and (d) SGH-Cu/TiO_2.

carbonate to formate. It is also apparent that the conduction band edge reduction potential became slightly less negative as the amount of rutile phase increased, suggesting the existence of band offset at the interface between anatase and rutile phase [72]. Although not measured in this work, this band offset between anatase and rutile helps improve electron-hole pair separation [73,74].

In addition to the band offset between anatase and rutile phases, the UPS data and the band gap energies of the Cu doped samples revealed the existence of another offset between TiO_2 and CuO. The E_{VBM} of copper-doped samples could not be determined spectroscopically because it was complicated by the presence of a mixture of Cu(I), Cu(II) and Ti(IV). Therefore, the standard band gap energy (1.7 eV) [75] and measured photoelectron core level of CuO was used to investigate the band offset at the interface between the CuO and TiO_2. This could also be done for standard Cu_2O.

Fig. 12 depicts the band offset in all the copper-doped samples prepared via sol-gel and incipient wetness methods. As shown on the XRD patterns for the sol gel copper doped TiO_2 photocatalysts that the copper is highly dispersed within the network of the TiO_2, therefore no band offset is formed. For both direct and indirect band gap energies, all the samples prepared via the incipient wetness method have shown the type I band offset, except for the indirect band gap energy of IW-Cu/SGL-TiO_2 where a type II was formed. Zhang, et al. [76] have extensively reviewed the different types of band offsets possible between semiconductors. In type I, both electron and holes accumulate in the conduction band and valence band of CuO respectively. The charge carriers easily recombine due to the small band gap energy of CuO (1.7 eV). Thus, type I does not promote charge separation. However, in type II, charge carriers are separated leading to an enhanced photocatalytic performance. According to the literature [77,78], Cu_2O is a p-type semiconductor with a more negative conduction band potential than both TiO_2 and CuO, hence coupling both Cu_2O, CuO and TiO_2 could lead to the formation of more stable charge separation due to the type II band offset.

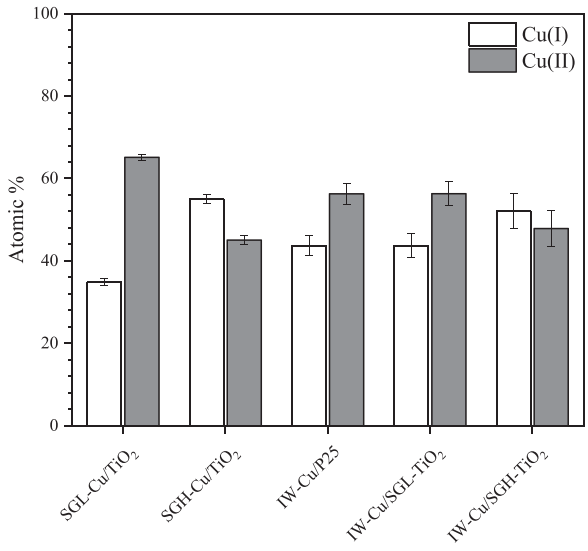

Fig. 10. Atomic ratios between Cu(II) and Cu(I).

3.2. Photocatalytic reduction of sodium bicarbonate/carbonate to formate

Photoreduction of sodium bicarbonate/carbonate cannot be conducted in acidic medium, because this will cause a shift in the equilibrium of the CO_2 solubilisation and ionisation reaction (8) towards the direction of dissolved CO_2 and H_2O. This will then lead to lower bicarbonate/carbonate concentrations, and potentially lead to CO_2 escaping out of solution as a gas, creating additional gas-liquid mass transfer constraints.

$$CO_2 + H_2O \overset{k_1}{\leftrightarrow} H^+ + HCO_3^- \overset{k_2}{\leftrightarrow} 2H^+ + CO_3^{2-} \quad (8)$$

Acidic media is also not compatible with Cu-doped photocatalysts as CuO is readily soluble in such solutions, making it impracticable to run the bicarbonate ion reduction in this medium. Therefore, all reactions were carried out at alkaline *pH*.

To study the copper leaching during the reaction on different copper loading (0.5, 1,3 and 6 wt%) on P25 and 5 wt% SGL-Cu/TiO_2 an inductively coupled plasma optical emission spectrometry (ICP-OES) was used. The analysis measured the concentration of copper in suspension before and after irradiation. As shown in the Supplementary Information S5, no significant leaching of copper was observed after irradiation.

3.2.1. Effect of catalyst synthesis method

The photocatalytic performance of the prepared photocatalyst samples was tested through conversion of sodium bicarbonate/carbonate buffer solutions to sodium formate, illuminated under UV–vis radiation. Control experiments were conducted to ensure that the reaction would exclusively occur when both light and catalyst were present. One control experiment was conducted in the absence of light, and another control experiment was conducted in the absence of photocatalyst. In both cases, no formate was detected, confirming that the reaction only proceeds through both light and catalyst activation.

The results for the full testing of all catalyst samples with light are shown in Fig. 13. All the pure-TiO_2 samples prepared in house, the P25 used as a benchmark, and the Cu-doped TiO_2 samples prepared both through sol-gel at *pH* 1.5 and by incipient wetness of the TiO_2 prepared by sol-gel at *pH* 1.5 showed no activity towards reduction of sodium bicarbonate to formate.

The SGH-TiO_2 was virtually 100% anatase (Table 4) and has an indirect band gap energy of 3.25 eV, while SGL-TiO_2 and P25 TiO_2 had an anatase to rutile ratio of 39%:61% and 80%:20% respectively, and indirect band gaps of 2.96 eV and 3.24 eV respectively. Anatase has been shown to have low photocatalytic activity compared to mixtures of anatase and rutile. Anatase and rutile phases usually form favourable type II band offsets as shown in Fig. 14. Scanlon, et al. [72] have shown that coexistence of anatase and rutile phases reduces the chances of charge carrier recombination by transferring electrons from the conduction band of the anatase phase to the conduction band of the rutile. On the other hand, the generated holes are being transferred from the valence band of the rutile phase to that of the anatase phase. Thus, the photocatalytic activity of P25 and SGL-TiO_2 is expected to be higher than SGH-TiO_2. However, as stated above, when performing the full testing of these catalyst samples with light, no photocatalytic activity towards reduction of sodium bicarbonate to formate was observed (Fig. 13). This can be attributed to the fast recombination of charge

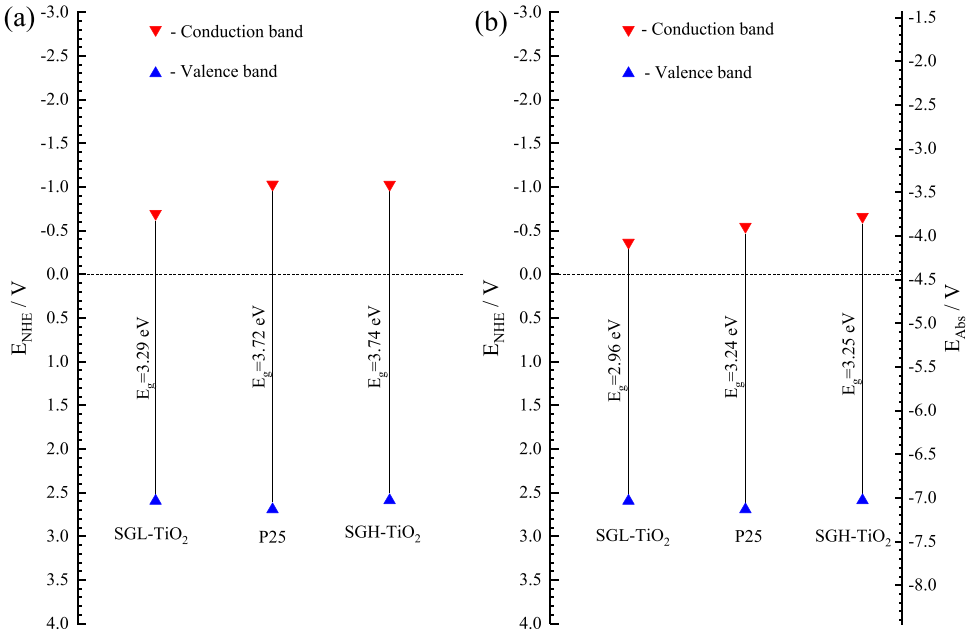

Fig. 11. (a) Direct and (b) indirect conduction band, valence band minimum, and indirect band gap energies of commercial and in-house TiO_2.

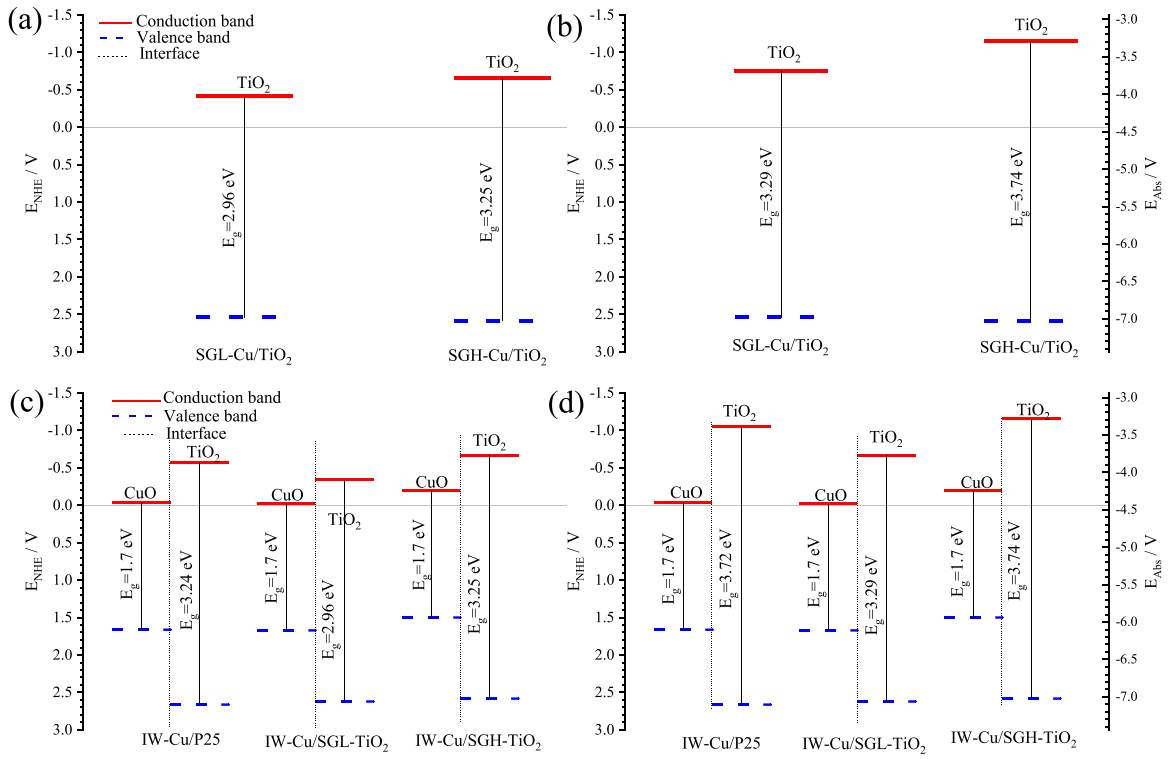

Fig. 12. Band offset at the interface between CuO and TiO_2 for (a, c) indirect and (b, d) direct band gap energies of the Cu doped samples prepared via (a,b) sol-gel (SG) and (c,d) incipient wetness methods (IW).

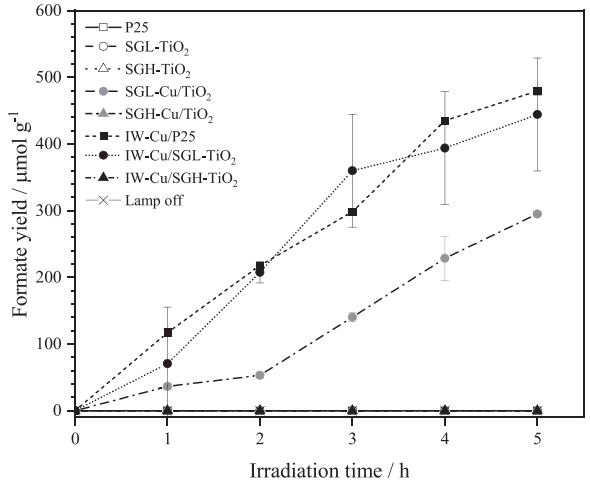

Fig. 13. Comparison of the performance of the different catalysts by studying the yield of formate at *pH* 8.34.

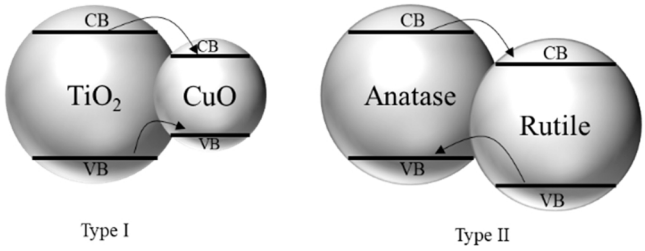

Fig. 14. Type I and II band offset.

carriers (i.e. recombination of the electrons and with the holes) which were initially generated in low density due to inefficient illumination of the reaction mixture. The inefficient illumination was caused by the spectrum of the light source (Supplementary Information S1) which can emit up to a little more than 4 eV and the intensity beyond this is likely not high enough to excite a high electron density in the samples with a high band gap energy. Furthermore, the photoreactor relative light intensity mapping (Supplementary Information S2) showed that only approximately 25% of the reaction mixture is efficiently illuminated at a time. As a result, few electrons are likely being generated with energy sufficient to participate in reducing the bicarbonate/carbonate ions, especially the SGH-TiO_2 and P25 with the direct band gap energy of 3.74 eV and 3.72 eV respectively.

Additionally, the high rutile content in SGL-TiO_2 may have had a detrimental effect on its photocatalytic activity. Colbeau-Justin, et al. [79] showed that the lifetime of the generated electrons in the rutile phase is shorter than in the anatase phase because of the difference in their effective masses which facilitate charge carrier transfer [80]. Su, et al. [81] established 3 ranges of anatase-rutile phase ratio with an optimum range between 0.67 and 4 to balance charge recombination effects with the formation of favourable type II band offsets.

The introduction of an electron trap can minimise the undesirable charge carrier recombination. The positive reduction potential of metal ions with respect to TiO_2 is indicative of their choice as electron trap. The reduction potential must be more positive than the band edge position of TiO_2. The standard redox potential of Cu ions shown in reaction (9), (10) and (11) makes it a good candidate in minimising charge carrier recombination [82]:

$$Cu^{2+} + e^- \rightarrow Cu^+, E^o = 0.17V \quad (9)$$

$$Cu^{2+} + 2e^- \rightarrow Cu^0, E^o = 0.34V \quad (10)$$

$$Cu^+ + e^- \rightarrow Cu^0, E^o = 0.52V \quad (11)$$

However, despite doping with Cu, the SGH-Cu/TiO_2 and IW-Cu/

SGH-TiO_2 showed no activity with respect to formate production. As mentioned in the subsection 3.1.4, SGH-Cu/TiO_2 formed no band offset while the band position of IW-Cu/SGH-TiO_2 showed the type I band offset between TiO_2 and CuO (Fig. 12). The band gap energy of CuO and Cu_2O is 1.7 eV (729 nm) and 2.2 eV (564 nm) respectively. In this work, a UV–visible light source was used, however under visible light irradiation, electrons will be excited to the conduction band of these oxides. Similarly, under UV irradiation, electrons and holes from the TiO_2 are respectively transitioned to the conduction band and the valence band of CuO [66], where the electron-hole pair accumulate and eventually recombine.

Additionally, as shown in Fig. 10, both samples have Cu(II) and Cu(I) coexisting, in the form of CuO and Cu_2O respectively, at almost equal ratio on the anatase phase. The high reduction potential of Cu(I) causes it to compete for electrons with surface adsorbed species leading to a decrease in charge carrier transfer. On the other hand, Cu(II) with its unfilled 3d orbital and moderate reduction potential can easily trap and transfer the electrons or become reduced to Cu(I) as demonstrated in reaction (12) [83].

$$Cu^{2+} \underset{O_2/H^+}{\overset{e^-}{\rightleftharpoons}} Cu^{+} \tag{12}$$

As shown in Fig. 13, formate production was observed when testing the Cu-doped in-house TiO_2 prepared through sol-gel at *pH* 0.4 (SGL-Cu/TiO_2) and the samples prepared via incipient wetness with the exception of the Cu impregnated TiO_2 prepared at *pH* 1.5. The shifting of the absorption spectrum through lowering the band gap energies of these samples via doping with Cu made it possible to increase their photocatalytic activity. Additionally, the presence of CuO, Cu_2O, anatase phase and rutile phase in these samples improve their charged carrier generation, transfer and stability, as the coexistence of these oxides is likely to form a mixture of type I and type II band offset depicted in Fig. 15. Upon illumination within the visible spectrum of light, high energy electrons from the conduction band of Cu_2O migrate to the conduction band of CuO. Likewise, upon illumination within UV spectrum, high energy electrons in the conduction band of the anatase phase migrate to the conduction band of both rutile phase and CuO. Similar band alignments were reported by Basnet, et al. [84] and Luna, et al. [85].

It should be noted that formate production was only detected when using catalyst samples doped with Cu containing a mixture of anatase and rutile phases, and being richer in Cu(II) than in Cu(I). Also, it was determined that a high content of copper on the surface, as shown by the ratio of Cu:Ti from the XPS data, is desirable. In aqueous solution under illumination, the presence of Cu(I) is not favourable because the reduction potential of Cu(I) exists within its band gap, resulting in photo corrosion [86]. Cu(II) and Cu(II)/Cu(I) mixtures were shown to be more stable compared to Cu(I) [87] and varying the relative composition of Cu(II)/Cu(I) determines which of the phases govern the charge carrier dynamics [88].

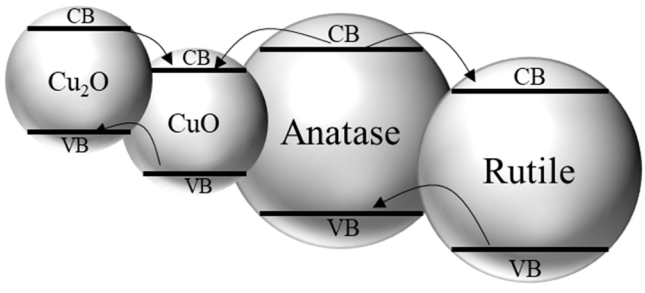

Fig. 15. Combination of type I and II band offsets.

The Cu doped samples prepared via the incipient wetness method have shown superior performance compared to the sample prepared via the sol-gel method. The catalyst activities shown in Fig. 13 can be ranked as SGL-Cu/TiO_2 < IW-Cu/SGL-TiO_2 ≈ IW-Cu/P25, corresponding to average reaction rates over 5 h of 59 μmol·g^{-1}·h^{-1}, 89 μmol·g^{-1}·h^{-1} and 96 μmol·g^{-1}·h^{-1} respectively at *pH* 8.34 (0.1 M sodium bicarbonate). In addition to the formation of a band offset and the presence of both anatase and rutile, the superiority of the incipient wetness method here could also be related to the average crystallite size and possible segregation of Cu. The average crystallite size of the anatase phase in SGL-TiO_2 prepared via the sol-gel method is 13.9 nm, while the crystallite size of the anatase phase in IW-Cu/SGL-TiO_2 and IW-Cu/P25 samples prepared via the incipient wetness method is 21.1 and 22.4 nm respectively. The crystallite size of the rutile phase in the latter samples remained unchanged (35.1 nm).

The presence of other organic species was not detected by HPLC, however it could not be disregarded. Yang, et al. [89] reported formation of formic acid alongside formaldehyde and methanol in photocatalytic reduction of sodium carbonate at *pH* = 3 on CuO doped TiO_2. Additionally, Zhang, et al. [90] reported formation of other products and significant decrease in formate concentration after almost 41 h of irradiation, suggesting that the process proceeds through a complex mechanism accompanied by formation of intermediate products. Kisch, et al. [91] reported that the bicarbonate photo-reduction to formate is accompanied by oxalate and formaldehyde formation through a series of complex pathways.

3.2.2. *Effect of reaction medium pH*

The *pH* of the 0.1 M sodium bicarbonate/carbonate solution was adjusted by varying the molar ratio of bicarbonate/carbonate ions in the solution. The chemistry of bicarbonate/carbonate buffer solutions is well established [92]. Some of the relevant reactions through which bicarbonate is reduced to formate and other products are shown below [93–95]:

$$Photocatalyst + h\nu \rightarrow e^-_{CB} + h^+_{VB} \tag{13}$$

$$H_2O + h^+_{VB} \rightarrow H^+ + \dot{O}H \tag{14}$$

$$HCO_3^- + 2e^- + 2H^+ \rightarrow HCO_2^- + H_2O \tag{15}$$

$$CO_3^{2-} + 2e^- + 3H^+ \rightarrow HCO_2^- + H_2O \tag{16}$$

$$HCO_3^- + \dot{O}H \rightarrow \dot{C}O_3^- + H_2O \tag{17}$$

$$CO_3^{2-} + \dot{O}H \rightarrow \dot{C}O_3^- + OH^- \tag{18}$$

$$2\dot{C}O_3^- + 2H^+ + 2e^- \rightarrow 2HCO_3^- \tag{19}$$

$$HCO_3^- + 2H^+ + 3e^- + h^+_{VB} \rightarrow HCO_2^- + H_2O \tag{20}$$

$$CO_3^{2-} + 3H^+ + 3e^- + h^+_{VB} \rightarrow HCO_2^- + H_2O \tag{21}$$

IW-Cu/P25 was the best performing catalyst in this study and therefore it was used to investigate the effect of the *pH* of the solution. Fig. 16 shows the formate production rate at different solvent *pH* values. As the *pH* increases from 8 to 11, the formate production rate increases from 96 to 173 μmol·g^{-1}·h^{-1}, and then dropping again when the *pH* is further increased to 12.

To explain this trend, it is important to understand how *pH* affects the adsorption of the bicarbonate and carbonate ions onto the catalyst surface. It is known that the surface charge of TiO_2 is a function of its crystalline phases [96] and that the amount of each phase has been shown to influence adsorption of substrates in photocatalytic degradation of azo-dyes [97] as explained herein. In aqueous solution, when the

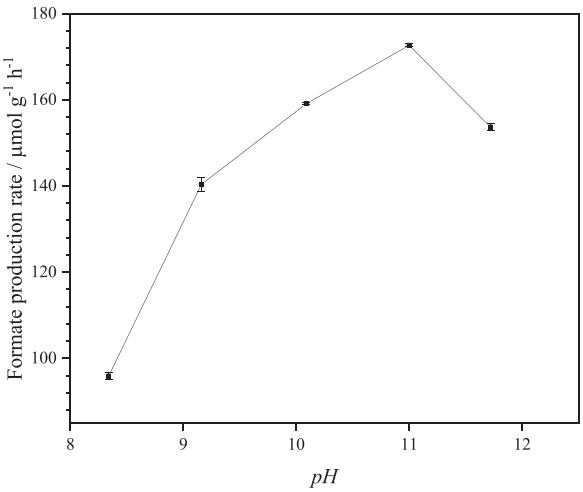

Fig. 16. Average rate of formate production at different *pH* on IW-Cu/P25 over a period of 5 h.

pH equals the *pH* of the point of zero charge (pH_{PZC}), the TiO_2 crystals surfaces exhibit terminal hydroxyl groups and bonded oxygen groups that can either be protonated or deprotonated depending on *pH* change [98] as shown in Fig. 17. At $pH < pH_{PZC}$, the hydroxyl group and bonded oxygen get protonated creating a positively charged surface. On the other hand, when $pH > pH_{PZC}$, the hydroxyl groups get deprotonated. Due to generation of surface charges as a function of *pH*, this will govern the adsorption of ions with opposite charges. Charged ions can be easily adsorbed or repelled due to electrostatic effects depending on their charge and the *pH* of the reaction medium, which dictates the charge of the surface.

The pH_{PZC} of TiO_2 lies within the range of neutral in the *pH* scale depending on the crystal phase composition [99] with an insignificant shift of the pH_{PZC} between anatase phase and rutile phase. In this study, on the basis of the reported pH_{PZC} of TiO_2 [97,100], it is thought that at $pH = 8.34$, the TiO_2 surface would have begun to deprotonate. In theory, this should lead to a reduction in the adsorption of bicarbonate ions onto the TiO_2 surface as these ions are negatively charged. This would be in good agreement with the findings of Ku, et al. [96]. However, alternative and complementary explanations have also suggested that the reaction proceeds through formation of a specific complex interaction between the photocatalyst surface supported by the dopant and the bicarbonate ion [101], making the attraction of the bicarbonate adsorption possible. Therefore, the trend observed can be justified by the mechanism of bicarbonate reduction through the formation of this specific complex interaction. This can also be supported by the fact that the reaction *pH* is known to significantly influence the band edge position of photocatalyst samples [98].

Also, when the *pH* of the reaction medium increases, the CO_2 reduction potential becomes more negative [102], influencing the thermodynamics of the photocatalytic reduction. In this study, *pH* 11 was established as the optimum to maximise the reduction of bicarbonate/carbonate ions to formate. At *pH* 8.34, the reaction medium is much richer in bicarbonate than carbonate ions. The reduction of HCO_3^- to HCO_2^- (reaction (15)) competes with its reduction to $\dot{C}O_3^-$ (reaction (17)),with reaction (18) reported to be a magnitude faster than reaction (17) [94]. As the *pH* increases, formate production starts being favoured through reaction (15) and reaction (16), thus the increase in the formate production rate. At *pH* 12 when the inorganic carbon is in the form of CO_3^{2-}, formate starts being formed only through reaction (16). Reactions (20) and (21) represent the overall stoichiometric reaction of bicarbonate and carbonate ions, respectively. The limitation to the use of bicarbonate and carbonate is that they were shown to act as hole scavengers [95,103]. However, at the same time this can be an advantage in improving charge carrier separation. The hole scavenging by HCO_3^- could serve as a source of excess of the H^+needed for the reduction of $CO_3^{2-}$to HCO_2^-. Hence, the decrease in formate production at *pH* 11.72 could also be explained by the low H^+ due to the hole scavenging by only CO_3^{2-}.

4. Conclusions

TiO_2 and Cu doped TiO_2 were successfully prepared via sol-gel and incipient wetness methods, and the effect of *pH* during the sol-gel preparation studied at *pH* 0.4 and 1.5. In this study it was demonstrated that *pH* plays an important role in catalyst preparation by controlling the formation of the TiO_2 phases and the distribution of Cu species. Increasing the synthesis *pH* of TiO_2 from 0.4 to 1.5 during sol-gel was shown to decrease the anatase to rutile phase transformation. Addition of the copper dopant via the sol-gel route has also inhibited anatase to rutile phase transformation as a result of the incorporation of the dopant in the network of TiO_2. However, doping via the incipient wetness method was shown to have no influence on phase transformation, possibly due to the segregation of the dopant. Within the margin of error of the measurements, crystallite size of the anatase phase remained within the same range on addition of copper via both synthesis methods. The crystallite size of the rutile phase also remained unchanged in both methods, except for the SGL-Cu/TiO_2 where the crystallite size decreased from 32.5 nm to 19.7 nm due to significant increase in the anatase to rutile phases ratio from 0.64 to 3.8. The direct and indirect band gap energy decreased by decreasing the *pH* during sol-gel synthesis from 1.5 to 0.4. Further decrease was recorded on introduction of Cu dopant. The XPS results revealed that Cu exists in the form of Cu(I) and Cu(II), with the samples prepared at low pH favouring Cu (II). The ratio of Cu(II) to Cu(I) in the samples prepared at *pH* 0.4 via sol-gel method was 4.9, while in the sample prepared via incipient wetness it was 2.6. In the samples prepared via the two methods at *pH* 1.5, there is almost equal amounts of Cu(I) and Cu(II). The bare TiO_2 prepared showed no activity towards CO_2 reduction, presumably due to a wider band gap and poor light distribution due to the photoreactor design. However, on doping, the light absorption of the Cu doped TiO_2 rich in anatase and rutile phases as well as high copper to titanium (Cu:Ti) ratio

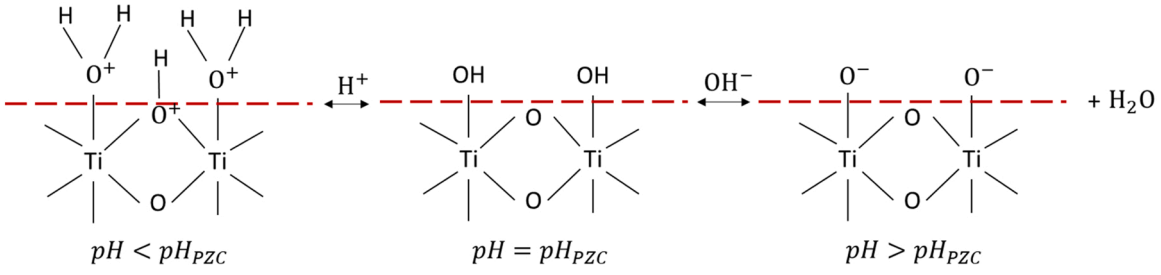

Fig. 17. Simplified scheme of protonated, electroneutral and deprotonated TiO_2 surface. Adapted from Beranek [98].

on the surface have shown photocatalytic activity. At the reaction *pH* of 8.4, the formate production rate is 59 μmol·g^{-1}·h^{-1}, 89 μmol·g^{-1}·h^{-1} and 96 μmol·g^{-1}·h^{-1} on SGL-Cu/TiO_2, IW-Cu/SGL-TiO_2 and IW-Cu/P25 respectively. The *pH* of the reaction medium was further optimised, raising the formate production rate on IW-Cu/P25 from 96 μmol·g^{-1}·h^{-1} to 176 μmol·g^{-1}·h^{-1} at *pH* 11.

Future work should be conducted to investigate the use of hole scavengers to improve the conversion to formate. Additionally, the use of synchrotron-based method for in-situ/operando analysis of the samples during the reaction in a wet form should also be considered in future studies. This would lead to a more comprehensive understanding of the behaviour of the photocatalyst samples and performance in specific reaction conditions.

CRediT authorship contribution statement

Abdullahi Adamu: Formal analysis, Funding acquisition, Investigation, Methodology, Validation, Visualization, Writing – original draft, Writing – review & editing. **Mark Isaacs:** Formal analysis, Investigation, Methodology, Resources, Writing – original draft. **Kamelia Boodhoo**: Conceptualization, Funding acquisition, Methodology, Project administration, Resources, Supervision, Validation, Writing – original draft, Writing – review & editing. **Fernando Russo Abegão:** Conceptualization, Formal analysis, Funding acquisition, Methodology, Project administration, Resources, Supervision, Validation, Visualization, Writing – original draft, Writing – review & editing.

Declaration of Competing Interest

The authors declare that they have no known competing financial interests or personal relationships that could have appeared to influence the work reported in this paper.

Data availability

Data will be made available on request.

Acknowledgements

Abdullahi Adamu would like to acknowledge the Petroleum Technology Development Fund (PTDF), Nigeria, for funding his postgraduate studies at Newcastle University under scholarship number PTDF/ED/PHD/AA/1127/17.

Appendix A. Supporting information

Supplementary data associated with this article can be found in the online version at doi:10.1016/j.jcou.2023.102428.

References

[1] K. Li, X. An, K.H. Park, M. Khraisheh, J. Tang, A critical review of CO_2 photoconversion: Catalysts and reactors, Catal. Today 224 (2014) 3–12.
[2] A. Nikokavoura, C. Trapalis, Alternative photocatalysts to TiO 2 for the photocatalytic reduction of CO 2, Appl. Surf. Sci. 391 (2017) 149–174.
[3] A. Adamu, F. Russo-Abegão, K. Boodhoo, Process intensification technologies for CO_2 capture and conversion – a review, BMC Chem. Eng. 2 (1) (2020).
[4] Y.Y. Lee, H.S. Jung, J.M. Kim, Y.T. Kang, Photocatalytic CO 2 conversion on highly ordered mesoporous materials: Comparisons of metal oxides and compound semiconductors, Appl. Catal. B: Environ. 224 (2018) 594–601.
[5] M. Tahir, N.S. Amin, Advances in visible light responsive titanium oxide-based photocatalysts for CO_2 conversion to hydrocarbon fuels, Energy Convers. Manag. 76 (2013) 194–214.
[6] Y.Y. Lee, H.S. Jung, Y.T. Kang, A review: Effect of nanostructures on photocatalytic CO 2 conversion over metal oxides and compound semiconductors, J. CO_2 Util. 20 (2017) 163–177.
[7] D.A.H. Hanaor, C.C. Sorrell, Review of the anatase to rutile phase transformation, J. Mater. Sci. 46 (4) (2010) 855–874.
[8] K. Rajeshwar, Fundamentals of Semiconductor Electrochemistry and Photoelectrochemistry, Semicond. Electrodes Photoelectrochem. 6 (2002) 1–52.
[9] C. Byrne, G. Subramanian, S.C. Pillai, Recent advances in photocatalysis for environmental applications, J. Environ. Chem. Eng. (2017).
[10] R.N. Grimes, Chapter 2 – Structure and Bonding, in: K. Birtcher (Ed.), Carboranes, John Fedor, 2016, pp. 7–18.
[11] B. Zhang, S. Cao, M. Du, X. Ye, Y. Wang, J. Ye, Titanium Dioxide (TiO2) Mesocrystals: Synthesis, Growth Mechanisms and Photocatalytic Properties, Catalysts 9 (1) (2019).
[12] L.E. Oi, M.-Y. Choo, H.V. Lee, H.C. Ong, S.B.A. Hamid, J.C. Juan, Recent advances of titanium dioxide (TiO2) for green organic synthesis, RSC Adv. 6 (110) (2016) 108741–108754.
[13] O. Carp, Photoinduced reactivity of titanium dioxide, Prog. Solid State Chem. 32 (1–2) (2004) 33–177.
[14] S. mo, W. Ching, Electronic and optical properties of three phases of titanium dioxide: Rutile, anatase, and brookite, Phys. Rev. B, Condens. Matter 51 (1995) 13023–13032.
[15] U. Diebold, The surface science of titanium dioxide, Surf. Sci. Rep. 48 (5) (2003) 53–229.
[16] Y. Hu, H.-L. Tsai, C.-L. Huang, Effect of brookite phase on the anatase-rutile transition in titania nanparticles, J. Eur. Ceram. Soc. 23 (2003) 691–696.
[17] B. Ohtani, O.O. Prieto-Mahaney, D. Li, R. Abe, What is Degussa (Evonik) P25? Crystalline composition analysis, reconstruction from isolated pure particles and photocatalytic activity test, J. Photochem. Photobiol. A: Chem. 216 (2–3) (2010) 179–182.
[18] T. Sumita, T. Yamaki, S. Yamamoto, A. Miyashita, Photo-induced surface charge separation of highly oriented TiO2 anatase and rutile thin films, Appl. Surf. Sci. 200 (1) (2002) 21–26.
[19] A. Sclafani, J.M. Herrmann, Comparison of the Photoelectronic and Photocatalytic Activities of Various Anatase and Rutile Forms of Titania in Pure Liquid Organic Phases and in Aqueous Solutions, The, J. Phys. Chem. 100 (32) (1996) 13655–13661.
[20] B. Tryba, J. Orlikowski, R.J. Wróbel, J. Przepiórski, A.W. Morawski, Preparation and Characterization of Rutile-Type TiO2 Doped with Cu, J. Mater. Eng. Perform. 24 (3) (2015) 1243–1252.
[21] A. Karami, Synthesis of TiO2 Nano Powder by the Sol-Gel Method and its Use as a Photocatalyst, J. Iran. Chem. Soc. 7 (2010) S154–S160.
[22] P. Nyamukamba, O. Okoh, H. Mungondori, R. Taziwa, S. Zinya, Synthetic Methods for Titanium Dioxide Nanoparticles: A Review, Titan. Dioxide - Mater. a Sustain. Environ. (2018).
[23] M. Hosseini, Zori, Synthesis of TiO2 Nanoparticles by Microemulsion/Heat Treated Method and Photodegradation of Methylene Blue, J. Inorg. Organomet. Polym. Mater. 21 (1) (2010) 81–90.
[24] J. Low, B. Cheng, J. Yu, Surface modification and enhanced photocatalytic CO 2 reduction performance of TiO 2: a review, Appl. Surf. Sci. 392 (2017) 658–686.
[25] A. Hernańdez-Ramírez, I. Medina-Ramírez, Semiconducting Materials, in: A. Hernańdez-Ramírez, I. Medina-Ramírez (Eds.), Photocatalytic Semiconductors, Synthesis, Characterisation and Environmental Applications, Springer International Publishing, Switzerland, 2015, pp. 1–40.
[26] S.A. Ansari, M.M. Khan, M.O. Ansari, M.H. Cho, Nitrogen-doped titanium dioxide (N-doped TiO2) for visible light photocatalysis, in: New Journal of Chemistry, 40, 2016, pp. 3000–3009.
[27] J.A. Oliveira, A.E. Nogueira, M.C.P. Gonçalves, E.C. Paris, C. Ribeiro, G.Y. Poirier, T.R. Giraldi, Photoactivity of N-doped ZnO nanoparticles in oxidative and reductive reactions, Appl. Surf. Sci. 433 (2018) 879–886.
[28] Y. Park, W. Kim, H. Park, T. Tachikawa, T. Majima, W. Choi, Carbon-doped TiO2 photocatalyst synthesized without using an external carbon precursor and the visible light activity, Appl. Catal. B: Environ. 91 (1–2) (2009) 355–361.
[29] O. Ola, M.M. Maroto-Valer, Transition metal oxide based TiO2 nanoparticles for visible light induced CO_2 photoreduction, Appl. Catal. A: Gen. 502 (2015) 114–121.
[30] M. Tahir, B. Tahir, N.A.S. Amin, Synergistic effect in plasmonic Au/Ag alloy NPs co-coated TiO2 NWs toward visible-light enhanced CO_2 photoreduction to fuels, Appl. Catal. B: Environ. 204 (2017) 548–560.
[31] P. Sangpour, F. Hashemi, A.Z. Moshfegh, Photoenhanced Degradation of Methylene Blue on Cosputtered M:TiO2 (M = Au, Ag, Cu) Nanocomposite Systems: A Comparative Study, J. Phys. Chem. C. 114 (33) (2010) 13955–13961.
[32] K. Bhattacharyya, G.P. Mane, V. Rane, A.K. Tripathi, A.K. Tyagi, Selective CO_2 Photoreduction with Cu-Doped TiO2 Photocatalyst: Delineating the Crucial Role of Cu-Oxidation State and Oxygen Vacancies, J. Phys. Chem. C. 125 (3) (2021) 1793–1810.
[33] I. Ganesh, P.P. Kumar, I. Annapoorna, J.M. Sumliner, M. Ramakrishna, N. Y. Hebalkar, G. Padmanabham, G. Sundararajan, Preparation and characterization of Cu-doped TiO2 materials for electrochemical, photoelectrochemical, and photocatalytic applications, Appl. Surf. Sci. 293 (2014) 229–247.
[34] B.-R. Chen, V.-H. Nguyen, J.C.S. Wu, R. Martin, K. Kočí, Production of renewable fuels by the photohydrogenation of CO_2: effect of the Cu species loaded onto TiO2 photocatalysts, Phys. Chem. Chem. Phys. 18 (6) (2016) 4942–4951.
[35] N. Seriani, C. Pinilla, Y. Crespo, Presence of Gap States at Cu/TiO2 Anatase Surfaces: Consequences for the Photocatalytic Activity, The, J. Phys. Chem. C. 119 (12) (2015) 6696–6702.
[36] H.W. Slamet, E. Nasution, S. Purnama, J. Kosela, Gunlazuardi, Photocatalytic reduction of CO_2 on copper-doped Titania catalysts prepared by improved-impregnation method, Catal. Commun. 6 (5) (2005) 313–319.
[37] S. Qin, F. Xin, Y. Liu, X. Yin, W. Ma, Photocatalytic reduction of CO_2 in methanol to methyl formate over CuO-TiO2 composite catalysts, J. Colloid Interface Sci. 356 (1) (2011) 257–261.

[38] S.S. Lee, H. Bai, Z. Liu, D.D. Sun, Novel-structured electrospun TiO2/CuO composite nanofibers for high efficient photocatalytic cogeneration of clean water and energy from dye wastewater, Water Res 47 (12) (2013) 4059–4073.

[39] S.S. Lee, H. Bai, Z. Liu, D.D. Sun, Optimization and an insightful properties—Activity study of electrospun TiO2/CuO composite nanofibers for efficient photocatalytic H2 generation, Appl. Catal. B: Environ. 140–141 (2013) 68–81.

[40] J.Fd Brito, M.V.B. Zanoni, On the application of Ti/TiO 2 /CuO n-p junction semiconductor: A case study of electrolyte, temperature and potential influence on CO 2 reduction, Chem. Eng. J. 318 (2017) 264–271.

[41] I.H. Tseng, W.-C. Chang, J.C.S. Wu, Photoreduction of CO_2 using sol–gel derived titania and titania-supported copper catalysts, Appl. Catal. B: Environ. 37 (1) (2002) 37–48.

[42] F. Fang, Y. Liu, X. Sun, C. Fu, Y. Prakash Bhoi, W. Xiong, W. Huang, TiO2 Facet-dependent reconstruction and photocatalysis of CuOx/TiO2 photocatalysts in CO_2 photoreduction, Appl. Surf. Sci. 564 (2021), 150407.

[43] L. Liu, C. Zhao, J.T. Miller, Y. Li, Mechanistic Study of CO_2 Photoreduction with H2O on Cu/TiO2 Nanocomposites by in Situ X-ray Absorption and Infrared Spectroscopies, The, J. Phys. Chem. C. 121 (1) (2017) 490–499.

[44] L. Liu, F. Gao, H. Zhao, Y. Li, Tailoring Cu valence and oxygen vacancy in Cu/TiO2 catalysts for enhanced CO_2 photoreduction efficiency, Appl. Catal. B: Environ. 134 135 (2013) 349–358.

[45] Y. Li, W.-N. Wang, Z. Zhan, M.-H. Woo, C.-Y. Wu, P. Biswas, Photocatalytic reduction of CO_2 with H2O on mesoporous silica supported Cu/TiO2 catalysts, Appl. Catal. B: Environ. 100 (1–2) (2010) 386–392.

[46] H.A. Schwarz, R.W. Dodson, Reduction potentials of CO_2- and the alcohol radicals, The, J. Phys. Chem. 93 (1) (1989) 409–414.

[47] T. Reda, C.M. Plugge, N.J. Abram, J. Hirst, Reversible interconversion of carbon dioxide and formate by an electroactive enzyme, Proc. Natl. Acad. Sci. (2008).

[48] E. Karamian, S. Sharifnia, On the general mechanism of photocatalytic reduction of CO_2, J. CO_2 Util. 16 (2016) 194–203.

[49] A. Olivo, V. Trevisan, E. Ghedini, F. Pinna, C.L. Bianchi, A. Naldoni, G. Cruciani, M. Signoretto, CO_2 photoreduction with water: Catalyst and process investigation, J. CO_2 Util. 12 (2015) 86–94.

[50] S. Shoji, G. Yin, M. Nishikawa, D. Atarashi, E. Sakai, M. Miyauchi, Photocatalytic reduction of CO_2 by Cu O nanocluster loaded SrTiO3 nanorod thin film, Chem. Phys. Lett. 658 (2016) 309–314.

[51] A.M. Selman, Z. Hassan, M. Husham, Structural and photoluminescence studies of rutile TiO2 nanorods prepared by chemical bath deposition method on Si substrates at different pH values, Measurement 56 (2014) 155–162.

[52] J. Xue, Q. Shen, F. Yang, W. Liang, X. Liu, Investigation on the influence of pH on structure and photoelectrochemical properties of CdSe electrolytically deposited into TiO2 nanotube arrays, J. Alloy. Compd. 607 (2014) 163–168.

[53] M.E. Simonsen, E.G. Søgaard, Sol–gel reactions of titanium alkoxides and water: influence of pH and alkoxy group on cluster formation and properties of the resulting products, J. Sol. -Gel Sci. Technol. 53 (3) (2010) 485–497.

[54] S.L. Isley, R.L. Penn, Titanium Dioxide Nanoparticles: Effect of Sol−Gel pH on Phase Composition, Particle Size, and Particle Growth Mechanism, The, J. Phys. Chem. C. 112 (12) (2008) 4469–4474.

[55] V. Bhalla, V. Khullar, H. Tyagi, Experimental investigation of photo-thermal analysis of blended nanoparticles (Al2O3/Co3O4) for direct absorption solar thermal collector, Renew. Energy 123 (2018) 616–626.

[56] D.G.-U.S. Roessler, Process Prep. Colloïd. Solut. (1954).

[57] S. Challagulla, K. Tarafder, R. Ganesan, S. Roy, Structure sensitive photocatalytic reduction of nitroarenes over TiO 2, Sci. Rep. 7 (1) (2017) 8783.

[58] X. Wang, L. Sø, R. Su, S. Wendt, P. Hald, A. Mamakhel, C. Yang, Y. Huang, B. B. Iversen, F. Besenbacher, The influence of crystallite size and crystallinity of anatase nanoparticles on the photo-degradation of phenol, J. Catal. 310 (2014) 100–108.

[59] K. Kočí, L. Obalová, L. Matějová, D. Plachá, Z. Lacný, J. Jirkovský, O. Šolcová, Effect of TiO2 particle size on the photocatalytic reduction of CO_2, Appl. Catal. B: Environ. 89 (3–4) (2009) 494–502.

[60] M. Sahu, K. Suttiponparnit, S. Suvachittanont, T. Charinpanitkul, P. Biswas, Characterization of doped TiO2 nanoparticle dispersions, Chem. Eng. Sci. 66 (15) (2011) 3482–3490.

[61] Y. Wang, W. Duan, B. Liu, X. Chen, F. Yang, J. Guo, The Effects of Doping Copper and Mesoporous Structure on Photocatalytic Properties of TiO2, J. Nanomater. 2014 (2014) 1–7.

[62] C. Byrne, L. Moran, D. Hermosilla, N. Merayo, Á. Blanco, S. Rhatigan, S. Hinder, P. Ganguly, M. Nolan, S.C. Pillai, Effect of Cu doping on the anatase-to-rutile phase transition in TiO2 photocatalysts: Theory and experiments, Appl. Catal. B: Environ. 246 (2019) 266–276.

[63] M. Mohamad, B. Ul Haq, R. Ahmed, A. Shaari, N. Ali, R. Hussain, A density functional study of structural, electronic and optical properties of titanium dioxide: Characterization of rutile, anatase and brookite polymorphs, Mater. Sci. Semicond. Process. 31 (2015) 405–414.

[64] A. Hagfeldt, M. Graetzel, Light-induced redox reactions in nanocrystalline systems, Chem. Rev. 95 (1) (1995) 49–68.

[65] A.M. Smith, S. Nie, Semiconductor nanocrystals: structure, properties, and band gap engineering, Acc. Chem. Res. 43 (2) (2010) 190–200.

[66] G. Li, N.M. Dimitrijevic, L. Chen, T. Rajh, K.A. Gray, Role of Surface/Interfacial Cu2+ Sites in the Photocatalytic Activity of Coupled CuO−TiO2 Nanocomposites, J. Phys. Chem. C. 112 (48) (2008) 19040–19044.

[67] L.A. Dahonog, M.S.D.C.D. Vega, M.D.L. Balela, pH-dependent synthesis of copper oxide phases by polyol method, J. Phys.: Conf. Ser. 1191 (2019), 012043.

[68] S.K. Ryu, W.K. Lee, S. Park, Thermal Decomposition of Hydrated Copper Nitrate [Cu(NO3)2·3H2O] on Activated Carbon Fibers, Carbon Lett. 5 (2004) 180–185.

[69] A.V. Nikam, A. Arulkashmir, K. Krishnamoorthy, A.A. Kulkarni, B.L.V. Prasad, pH-Dependent Single-Step Rapid Synthesis of CuO and Cu2O Nanoparticles from the Same Precursor, Cryst. Growth Des. 14 (9) (2014) 4329–4334.

[70] R. López, R. Gómez, M.E. Llanos, Photophysical and photocatalytic properties of nanosized copper-doped titania sol–gel catalysts, Catal. Today 148 (1) (2009) 103–108.

[71] G. Colón, M. Maicu, M.C. Hidalgo, J.A. Navío, Cu-doped TiO2 systems with improved photocatalytic activity, Appl. Catal. B: Environ. 67 (1) (2006) 41–51.

[72] D.O. Scanlon, C.W. Dunnill, J. Buckeridge, S.A. Shevlin, A.J. Logsdail, S. M. Woodley, C.R. Catlow, M.J. Powell, R.G. Palgrave, I.P. Parkin, G.W. Watson, T. W. Keal, P. Sherwood, A. Walsh, A.A. Sokol, Band alignment of rutile and anatase TiO(2), Nat. Mater. 12 (9) (2013) 798–801.

[73] D.C. Hurum, A.G. Agrios, K.A. Gray, T. Rajh, M.C. Thurnauer, Explaining the Enhanced Photocatalytic Activity of Degussa P25 Mixed-Phase TiO2 Using EPR, The, J. Phys. Chem. B 107 (19) (2003) 4545–4549.

[74] A. Li, Z. Wang, H. Yin, S. Wang, P. Yan, B. Huang, X. Wang, R. Li, X. Zong, H. Han, C. Li, Understanding the anatase–rutile phase junction in charge separation and transfer in a TiO2 electrode for photoelectrochemical water splitting, Chem. Sci. 7 (9) (2016) 6076–6082.

[75] Y. Xu, M.A.A. Schoonen, The absolute energy positions of conduction and valence bands of selected semiconducting minerals, Am. Mineral. 85 (3–4) (2000) 543–556.

[76] L. Zhang, M. Jaroniec, Toward designing semiconductor-semiconductor heterojunctions for photocatalytic applications, Appl. Surf. Sci. 430 (2018) 2–17.

[77] W. Zhao, C. Liu, Mesoporous Cu–Cu2O@TiO2 heterojunction photocatalysts derived from metal–organic frameworks, RSC Adv. 10 (25) (2020) 14550–14555.

[78] H. Xu, S. Ouyang, L. Liu, D. Wang, T. Kako, J. Ye, Porous-structured Cu2O/TiO2 nanojunction material toward efficient CO_2 photoreduction, Nanotechnology 25 (16) (2014), 165402.

[79] C. Colbeau-Justin, M. Kunst, D. Huguenin, Structural influence on charge-carrier lifetimes in TiO2 powders studied by microwave absorption, J. Mater. Sci. 38 (11) (2003) 2429–2437.

[80] J. Zhang, P. Zhou, J. Liu, J. Yu, New understanding of the difference of photocatalytic activity among anatase, rutile and brookite TiO2, Phys. Chem. Chem. Phys. 16 (38) (2014) 20382–20386.

[81] R. Su, R. Bechstein, L. Sø, R.T. Vang, M. Sillassen, B. Esbjörnsson, A. Palmqvist, F. Besenbacher, How the Anatase-to-Rutile Ratio Influences the Photoreactivity of TiO2, The, J. Phys. Chem. C. 115 (49) (2011) 24287–24292.

[82] H. Abdullah, M.M.R. Khan, H.R. Ong, Z. Yaakob, Modified TiO 2 photocatalyst for CO 2 photocatalytic reduction: An overview, J. CO_2 Util. 22 (2017) 15–32.

[83] H. Nasution, E. Purnama, S. Kosela, J. Gunlazuardi, Photocatalytic reduction of CO on copper-doped Titania catalysts prepared by improved-impregnation method, Catal. Commun. 6 (5) (2005) 313–319.

[84] P. Basnet, E. Anderson, Y. Zhao, Hybrid CuxO–TiO2 Nanopowders Prepared by Ball Milling for Solar Energy Conversion and Visible-Light-Induced Wastewater Treatment, ACS Appl. Nano Mater. 2 (4) (2019) 2446–2455.

[85] A.L. Luna, M.A. Valenzuela, C. Colbeau-Justin, P. Vázquez, J.L. Rodriguez, J. R. Avendaño, S. Alfaro, S. Tirado, A. Garduño, J.M. De, la Rosa, Photocatalytic degradation of gallic acid over CuO–TiO2 composites under UV/Vis LEDs irradiation, Appl. Catal. A: Gen. 521 (2016) 140–148.

[86] A. Paracchino, V. Laporte, K. Sivula, M. Gratzel, E. Thimsen, Highly active oxide photocathode for photoelectrochemical water reduction, Nat. Mater. 10 (6) (2011) 456–461.

[87] P. Basnet, Y. Zhao, Tuning the CuxO nanorod composition for efficient visible light induced photocatalysis, Catal. Sci. Technol. 6 (7) (2016) 2228–2238.

[88] L. Shenje, S. Larson, Y. Zhao, S. Ullrich, Composition Effects on Ultrafast Optical Properties of CuxOy Thin Films: A Transient Absorption Study, The, J. Phys. Chem. C. 124 (45) (2020) 24908–24918.

[89] X. Yang, T. Xiao, P.P. Edwards, The use of products from CO_2 photoreduction for improvement of hydrogen evolution in water splitting, Int. J. Hydrog. Energy 36 (11) (2011) 6546–6552.

[90] X.V. Zhang, S.T. Martin, C.M. Friend, M.A.A. Schoonen, H.D. Holland|, Mineral-Assisted Pathways in Prebiotic Synthesis: Photoelectrochemical Reduction of Carbon(+IV) by Manganese Sulfide, JACS 126 (2004) 11247–11253.

[91] H. Kisch, P. Lutz, Photoreduction of bicarbonate catalyzed by supported cadmium sulfideDedicated to Professor Gottfried Huttner on the occasion of his 65th birthday, Photochem. Photobiol. Sci. 1 (4) (2002) 240–245.

[92] O. Pedersen, T.D. Colmer, K. Sand-Jensen, Underwater photosynthesis of submerged plants – recent advances and methods, Front. Plant Sci. 4 (2013).

[93] H. Pan, A. Steiniger, M.D. Heagy, S. Chowdhury, Efficient production of formic acid by simultaneous photoreduction of bicarbonate and oxidation of glycerol on gold-TiO 2 composite under solar light, J. CO_2 Util. 22 (2017) 117–123.

[94] A. Kumar, N. Mathur, Photocatalytic degradation of aniline at the interface of TiO2 suspensions containing carbonate ions, J. Colloid Interface Sci. 300 (1) (2006) 244–252.

[95] A. Corma, H. Garcia, Photocatalytic reduction of CO_2 for fuel production: Possibilities and challenges, J. Catal. 308 (2013) 168–175.

[96] Y. Ku, W.-H. Lee, W.-Y. Wang, Photocatalytic reduction of carbonate in aqueous solution by UV/TiO2 process, J. Mol. Catal. A: Chem. 212 (1–2) (2004) 191–196.

[97] E. Kordouli, K. Bourikas, A. Lycourghiotis, C. Kordulis, The mechanism of azo-dyes adsorption on the titanium dioxide surface and their photocatalytic degradation over samples with various anatase/rutile ratios, Catal. Today 252 (2015) 128–135.

[98] R. Beranek, Photo)electrochemical Methods for the Determination of the Band Edge Positions of TiO2-Based Nanomaterials, Adv. Phys. Chem. 2011 (2011) 1–20.
[99] M. Kosmulski, The significance of the difference in the point of zero charge between rutile and anatase, Adv. Colloid Interface Sci. 99 (3) (2002) 255–264.
[100] F. Azeez, E. Al-Hetlani, M. Arafa, Y. Abdelmonem, A.A. Nazeer, M.O. Amin, M. Madkour, The effect of surface charge on photocatalytic degradation of methylene blue dye using chargeable titania nanoparticles, Sci. Rep. 8 (1) (2018) 7104.
[101] K. Bourikas, C. Kordulis, A. Lycourghiotis, The Role of the Liquid-Solid Interface in the Preparation of Supported Catalysts, Catal. Rev. 48 (4) (2006) 363–444.
[102] Y. Hori, S. Suzuki, Electrolytic reduction of carbon dioxide at mercury electrode in aqueous solution, Bull. Chem. Soc. Jpn. 55 (3) (1982) 660–665.
[103] N.M. Dimitrijevic, B.K. Vijayan, O.G. Poluektov, T. Rajh, K.A. Gray, H. He, P. Zapol, Role of Water and Carbonates in Photocatalytic Transformation of CO_2 to CH4 on Titania, J. Am. Chem. Soc. 133 (11) (2011) 3964–3971.